AGU PUBLICATIONS

JGR

Journal of Geophysical Research: Oceans

RESEARCH ARTICLE

10.1002/2016JC011975

Key Points:

- A new Tidal and Subtidal (TST) OBC mitigates the dynamic inconsistencies for the flow concurrently driven tidal and subtidal forcing
- Decomposition of the solution into global and local solutions, and into tidal and subtidal components are effective in the TST OBC
- Resolving respective phases of tidal current, subtidal inflow/outflow, and other disturbances at open boundary is important in the TST OBC

Correspondence to:
J. Gan,
magan@ust.hk

Citation:
Liu, Z., and J. Gan (2016), Open boundary conditions for tidally and subtidally forced circulation in a limited-area coastal model using the Regional Ocean Modeling System (ROMS), *J. Geophys. Res. Oceans*, *121*, doi:10.1002/2016JC011975.

Received 19 MAY 2016
Accepted 22 JUL 2016
Accepted article online 2 AUG 2016

Open boundary conditions for tidally and subtidally forced circulation in a limited-area coastal model using the Regional Ocean Modeling System (ROMS)

Zhiqiang Liu[1] and Jianping Gan[1]

[1]Department of Mathematics and Division of Environment, Hong Kong University of Science and Technology, Clear Water Bay, Kowloon, Hong Kong

Abstract In limited-area ocean models, open boundary conditions (OBCs) often create dynamic inconsistencies and perform poorly in resolving tidal or subtidal flow when both forces exist. Orlanski-type radiation OBCs are reasonably efficient at treating the subtidally forced flow, and *Flather*-type OBCs are commonly adapted for the tidally forced flow. However, neither of them performs well when tidal and subtidal forces simultaneously drive the flows. We have developed a novel OBC that integrates the active OBC in Gan and Allen (2005) and a Flather-type OBC. This new OBC accommodates the concurrent Tidal and Subtidal (TST) forcing, and the respective tidal or subtidal forcing, at the open boundary of a limited-area model. This new TST-OBC treats the tidal component with a Flather-type OBC, and it separates subtidal barotropic and baroclinic components into local (forced) and global (unforced) components. Then an unforced Orlanski-type OBC can be applied to the global part. We applied the TST-OBC to all model variables to reduce dynamic inconsistence. Using the Regional Ocean Modeling System, we applied the TST-OBC to the shallow East China Sea shelf where strong tidal and subtidal forces over complex topography govern the circulation. Our numerical experiments and analyses suggest that the TST-OBC was robust for both concurrent tidal-subtidal forcing and solely tidal or subtidal forcing at the open boundary. It reduced spurious energy reflection, and, overall, it performed better than an Orlanski-type or Flather-type OBC in reproducing realistic tidal and subtidal shelf circulation.

1. Introduction

The open boundary condition (OBC) in limited-area oceanic modeling is an “ill-posed” problem according to *Oliger and Sundstrom* [1978]. The simplified mathematics and reduced physics lead to a spurious reflection of disturbances at the open boundary (OB) and a deterioration of the interior solution. This deterioration is more likely to be amplified in realistic coastal ocean models where multiscale processes are concurrently modulated by tidal and subtidal forces over shallow waters. OBCs are meant to empower “a consistent specification of physical properties at the interface between the interior and the exterior of the computational domain” [*Gan and Allen*, 2005]. However, the task of perfecting OBCs, and reaching consensus of which OBCs to use has not been achieved.

The Orlanski-type [*Orlanski*, 1976] and Flather-type [*Flather*, 1976] conditions are the most widely used OBCs in ocean models. These two types of OBCs evolved from the radiation condition proposed by *Sommerfeld* [1949], who rationalized that the cross-boundary information propagates as nondispersive, unforced shallow water waves. Taking the barotropic velocity $\bar{U}$ as an example, the formulation of the radiation condition can be expressed as:

$$\bar{U}_t + C\bar{U}_N = 0, \tag{1}$$

where C is the propagation speed of $\bar{U}$, and t is time. N represents the coordinate normal to the OB. The subscripts denote partial differentiation.

Two categories of radiation OBCs have been commonly used: “active” and “passive” ones. These boundary conditions are associated with the determination and treatment of propagating disturbances. The “passive” OBCs determine the flow condition at the OB through the interior circulation, and they are only valid without forcing at the OB. The "active" OBCs include the integration of a priori specified outer information or "*external data*" [*Blayo and Debreu*, 2005] into the limited-area computational domain. The "active" OBCs are obviously needed in cases when there is forcing at the boundary.

The "active" OBC by *Marchesiello et al*. [2001] has been widely used for simulating subtidal circulation within the community of users of the Regional Ocean Modeling System (ROMS) [*Shchepetkin and McWilliams*, 2005]. This OBC considers inward and outward propagating information separately, and it utilizes a "passive" two-dimensional radiation condition, with variable propagation phase speed (*C*) to transmit the outward propagating disturbances that arrive at the OBs. A stronger nudging toward "*external data*" that are from observations or larger-scale simulations is applied to solutions associated with the inward propagating disturbances.

Considering the unforced nature in the radiation condition derived from equation (1), *Roed and Smedstad* [1984] proposed an "active" OBC by separating the total $\bar{U}$ in equation (1) into "local" ($\bar{U}_l$) and "global" ($\bar{U}_g$) solutions:

$$\bar{U}= \bar{U}_l+\bar{U}_g. \tag{2}$$

The "local" solution, $\bar{U}_l$, represents the forced "*external data*," while the unforced disturbances associated with the "global" solution, $\bar{U}_g$, is transmitted through the OB by an imposed radiation condition. The phase speed (inflow/ouflow), *C*, in equation (1), is solely determined by the "global" solution, $\bar{U}_g$, to satisfy the unforced condition in the equation. This scheme suppresses the spurious reflection of disturbances [*Perkins et al*., 1997].

Gan and Allen [2005] extended the approach of this variable separation to all variables in the governing equations of the model to ensure dynamic consistency, and to effectively reduce the discontinuity between interior and exterior solutions across the OB. This scheme has proved to be efficient in subtidally driven coastal circulation in a limited-area simulation based on either the Princeton Ocean Model (POM) [*Gan et al*., 2005] or ROMS [*Gan et al*., 2009a,2009b; *Pringle and Dever*, 2009].

When forcing is simultaneously subtidal and tidal, a Flather-type condition (FLA-OBC) has been commonly used in coastal and shelf circulation models. The FLA-OBC evolved from a scheme developed by *Reid and Bodine* [1968]. They represented the cross-boundary propagation of disturbances as surface gravity waves, or $\bar{U}=\sqrt{g/h}(\eta-\eta_l)$. *h* is water depth, and η is the resultant surface elevation at the OB. η_l represents the elevation displacement due to tidal forcing. This scheme induced a remarkable discrepancy in the simulated tidal amplitude and phase. *Flather* [1976] included the tidal current in the scheme to overcome these drawbacks, and this inclusion formed the widely adopted current FLA-OBC.

In the FLA-OBC, the "*external data*" are provided by the predicted tidal elevation (η_{Tlb}^{n+1}) and velocity ($\bar{U}_{Tlb}^{n+1}$). The subtidal circulation, (η_{Rlb}^{n+1}, $\bar{U}_{Rlb}^{n+1}$), are from, for example, large-scale oceanic models or observations. The FLA-OBC can be expressed by:

$$\bar{U}_b^{n+1}=\bar{U}_{Tlb}^{n+1}+\bar{U}_{Rlb}^{n+1}\pm\sqrt{\frac{g}{H}}\left(\eta_b^{n+1}-\eta_{Tlb}^{n+1}-\eta_{Rlb}^{n+1}\right). \tag{3}$$

(η_b^{n+1}, $\bar{U}_b^{n+1}$) are the resultant surface elevation and depth-averaged velocity perpendicular to the OB. The superscript, n, is the current time level, and the subscripts, *b*, *R*, *T*, and *l*, denote the grid point at the OB, residual (subtidal), tidal, and local components, respectively. *g* is the gravitational acceleration, and *H* refers to the total water depth. This scheme performed satisfactorily in the coastal circulation when the model was solely driven by tidal forcing [*Carter and Merrifield*, 2007].

The FLA-OBC has also been widely used in the barotropic velocity of regional oceanic models that are exclusively driven by subtidal forcing in the absence of η_{Tlb}^{n+1} and $\bar{U}_{Tlb}^{n+1}$ in equation (3). It has been "well-posed" for the two-dimensional linearized inviscid shallow water equation [*Blayo and Debreu*, 2005], and the outcomes are usually different from those obtained from the Orlanski-type condition. *Blayo and Debreu* [2005] and *Mason et al*. [2010] further developed the FLA-OBC by properly adapting the incoming variables to ensure consistency between the model solution and the "*external data*". The adaptation preserved the "*characteristic*" in the two-dimensional linearized inviscid equation.

These schemes are presently adapted in ROMS and perform well in two-way and one-way embedding applications [*Mason et al*., 2010]. However, these conditions in ROMS are designed for solutions in the barotropic mode in the ROMS kernel, and the radiation condition is usually used for solutions in the baroclinic mode. Thereby, inconsistent OBC schemes have been used for barotropic and baroclinic velocities and active tracers.

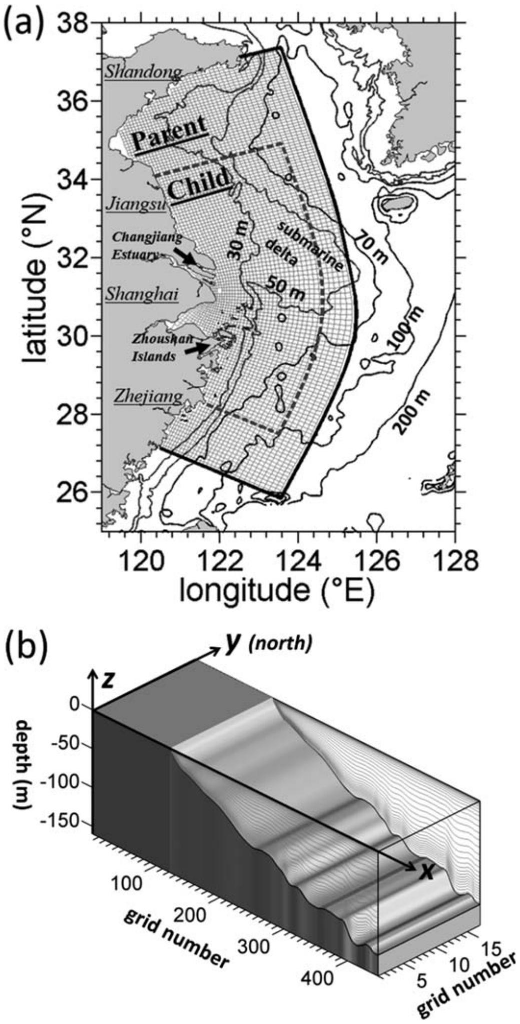

Figure 1. (a) Model curvilinear grid (every 10th grid line plotted) and bathymetry with the 30, 50, 70, 100, and 200 m isobaths shown. The parent domain, containing two OBs, was sketched by the bold and solid lines, whilst the child domain was bordered by the dashed lines in Figure 1a. Three-dimensional visualization of the submodel at the southern OB of the parent experiment was shown in (b). The vertical stretched terrain-following grid in *s*-coordinate was exhibited by the thin, grey lines in Figure 1b, also.

Meanwhile, the FLA-OBC by *Mason et al*. [2010] in ROMS (Rutgers version) mainly considered the propagation of external gravity waves with phase speed, $C=\sqrt{gH}$. This specified phase speed in the FLA-OBC cannot well transmit disturbances with different frequencies across the OB [*Oddo and Pinardi*, 2008], especially when the model is jointly driven by complex tidal and subtidal forces, or when it is experiencing strong nonlinearity.

A novel "active" OBC is needed that can jointly accommodate both the Tidal and Subtidal (TST) forces at the OB of a limited-area ocean model. This TST scheme should concurrently transmit the slow subtidal (with variable *C*) and fast tidal (with fixed *C*) components of the propagating disturbances, and the new scheme should allow a dynamically consistent treatment of all model variables. In this study, we examined comprehensively the performance of a new TST-OBC in a limited-area circulation model over the continental shelf of the East China Sea (ECS, Figure 1), where both tidal and subtidal forcing are critical to the shelf circulation. The outline of this paper is as follows. In section 2, we present the TST-OBC formulation. We introduce the model domain and topography in the ECS in section 3. In section 4, we validate the effectiveness of the new OBC by comparing the ECS results from a vast-area shelf simulation with those that were computed from a limited-area coastal model using the TST-OBC. In section 5, we investigate the TST-OBC's performance in downscaling applications under realistic forcing circumstances of the ECS. We provide conclusions in section 6.

2. TST-OBC Formulation

In this section, we introduce the formulae of the TST-OBC scheme, and we summarize the details in Table 1. For our study, we used the ROMS (Rutgers version), with three-dimensional hydrostatic primitive equations, to examine the TST-OBC scheme.

The core of the TST-OBC scheme includes: (1) treating the slow subtidal (variable phase speed) and fast tidal (fixed phase speed) components of the propagating disturbances separately; (2) separating the variables in the OB into local and global solutions and determining the phase speed in the radiation condition from the global part of the variables; and (3) using a similar OBC scheme for barotropic and baroclinic variables to preserve the dynamic consistency.

2.1. Barotropic Currents

We decomposed the velocities and surface elevation at the OBs into tidal and subtidal components, and this decomposition was proven to be effective in *Herzfeld and Gillibrand* [2015]. $\left(\bar{U}_{Tb}^{n+1},\ \bar{U}_{Rb}^{n+1}\right)$ and $\left(\bar{V}_{Tb}^{n+1},\bar{V}_{Rb}^{n+1}\right)$ represent the cross and along-OB velocities at the OB, respectively.

The TST-OBC involves using tidal and subtidal forcing. Table 2 demonstrates the procedure used to retrieve the forcing from "*external data*." In this study, we embedded a small (child) domain within a bigger (parent) domain and connected them by the TST-OBC to examine the performance of the OBC (see section 3). In this

Table 1. Summary of the TST-OBC Formulation[a]

	Barotropic Velocity ($\bar{U}_b^{n+1}, \bar{V}_b^{n+1}$)		
Surface Elevation η_b^{n+1}	*cross-OB velocity* ($\bar{U}_b^{n+1}$)		*Along-OB Velocity* ($\bar{V}_b^{n+1}$)
$\eta_b^{n+1}=\eta_{b\pm1}^{n+1}$	$\bar{U}_{Rb}^{n}=\bar{U}_b^{n}-\left(\bar{U}_{Tlb}^{n+1}\pm\sqrt{\frac{g}{H}}(\eta_b^{n+1}-\eta_{Tlb}^{n+1}-\eta_{Rlb}^{n+1})\right)$ $\begin{cases}\bar{U}_{R(b\pm1)}^{n+1}=\bar{U}_{(b\pm1)}^{n+1}-\bar{U}_{Tl(b\pm1)}^{n+1}\\ \bar{U}_{R(b\pm2)}^{n+1}=\bar{U}_{(b\pm2)}^{n+1}-\bar{U}_{Tl(b\pm2)}^{n+1}\end{cases}$ $\begin{cases}\bar{U}_{R(b\pm1)}^{n+1}=\bar{U}_{(b\pm1)}^{n+1}-\bar{U}_{Tl(b\pm1)}^{n+1}\\ \bar{U}_{R(b\pm2)}^{n+1}=\bar{U}_{(b\pm2)}^{n+1}-\bar{U}_{Tl(b\pm2)}^{n+1}\end{cases}$ $\begin{cases}\bar{U}_{Rg(b\pm1)}^{n}=\bar{U}_{R(b\pm1)}^{n}-\bar{U}_{Rlb}^{n}\\ \bar{U}_{Rg(b\pm1)}^{n+1}=\bar{U}_{R(b\pm1)}^{n+1}-\bar{U}_{Rlb}^{n+1}\\ \bar{U}_{Rg(b\pm2)}^{n+1}=\bar{U}_{R(b\pm2)}^{n+1}-\bar{U}_{Rlb}^{n+1}\end{cases}$ $C_g=\frac{\bar{U}_{Rg(b\pm1)}^{n}-\bar{U}_{Rg(b\pm1)}^{n+1}}{\bar{U}_{Rg(b\pm1)}^{n}-\bar{U}_{Rg(b\pm2)}^{n+1}}$		$\bar{V}_b^{n+1}=\bar{V}_{b\pm1}^{n+1}$
	$C_g<0$	$C_g\geq0$	
	$\bar{U}_b^{n+1}=$ $\bar{U}_{Rb}^{n}-\frac{\Delta t}{\lambda}(\bar{U}_{Rb}^{n}-\bar{U}_{Rlb}^{n})$ $+\bar{U}_{Tlb}^{n+1}\pm\sqrt{\frac{g}{H}}(\eta_b^{n+1}-\eta_{Tlb}^{n+1}-\eta_{Rlb}^{n+1})$	$\bar{U}_b^{n+1}=$ $\bar{U}_{Rlb}^{n+1}+\frac{1}{1+C_g}\left(\bar{U}_{Rgb}^{n}+C_g\bar{U}_{Rg(b\pm1)}^{n+1}\right)$ $+\bar{U}_{Tlb}^{n+1}\pm\sqrt{\frac{g}{H}}(\eta_b^{n+1}-\eta_{Tlb}^{n+1}-\eta_{Rlb}^{n+1})$	

Baroclinie Velocity ($\boldsymbol{U_b^{n+1}}, \boldsymbol{V_b^{n+1}}$).				
cross-OB velocity (U_b^{n+1})		*along-OB velocity* (V_b^{n+1})	*Active Tracers* (T_b^{n+1})	
$U_{Rb}^{n}=U_b^{n}-\bar{U}_{Tlb}^{n}$ $\begin{cases}U_{R(b\pm1)}^{n}=U_{(b\pm1)}^{n}-\bar{U}_{Tl(b\pm1)}^{n}\\ U_{R(b\pm2)}^{n}=U_{(b\pm2)}^{n}-\bar{U}_{Tl(b\pm2)}^{n}\end{cases}$ $\begin{cases}U_{R(b\pm1)}^{n+1}=U_{(b\pm1)}^{n+1}-\bar{U}_{Tl(b\pm1)}^{n+1}\\ U_{R(b\pm2)}^{n+1}=U_{(b\pm2)}^{n+1}-\bar{U}_{Tl(b\pm2)}^{n+1}\end{cases}$ $\begin{cases}U_{Rg(b\pm1)}^{n}=U_{R(b\pm1)}^{n}-U_{Rlb}^{n}\\ U_{Rg(b\pm1)}^{n+1}=U_{R(b\pm1)}^{n+1}-U_{Rlb}^{n+1}\\ U_{Rg(b\pm2)}^{n+1}=U_{R(b\pm2)}^{n+1}-U_{Rlb}^{n+1}\end{cases}$ $C_g=\frac{U_{Rg(b\pm1)}^{n}-U_{Rg(b\pm1)}^{n+1}}{U_{Rg(b\pm1)}^{n+1}-U_{Rg(b\pm2)}^{n+1}}$		$V_b^{n+1}=V_{b\pm1}^{n+1}$	$\begin{cases}T_{gb}^{n}=T_b^{n}-T_b^{n}\\ T_{g(b\pm1)}^{n+1}=T_{(b\pm1)}^{n+1}-T_{lb}^{n+1}\\ T_{g(b\pm2)}^{n+1}=T_{(b\pm2)}^{n+1}-T_{lb}^{n+1}\end{cases}$ $C_g=\frac{T_{g(b\pm1)}^{n}-T_{g(b\pm1)}^{n+1}}{T_{g(b\pm1)}^{n+1}-T_{g(b\pm2)}^{n+1}}$	
$C_g<0$	$C_g\geq0$		$C_g<0$	$C_g\geq0$
$U_b^{n+1}=$ $U_{Rb}^{n}-\frac{\Delta t}{\lambda}(U_{Rb}^{n}-U_{Rlb}^{n})$ $+\bar{U}_{Tlb}$	$U_b^{n+1}=$ $U_{Rlb}^{n+1}+\frac{1}{1+C_g}\left(U_{Rgb}^{n}+C_gU_{Rg(b\pm1)}^{n+1}\right)$ $+\bar{U}_{Tlb}$		$T_b^{n+1}=$ $T_b^{n}-\frac{\Delta t}{\lambda}(T_b^{n}-T_{lb}^{n})$	$T_b^{n+1}=$ $T_{lb}^{n+1}+\frac{1}{1+C_g}\left(T_{gb}^{n}+C_gT_{b(b\pm1)}^{n+1}\right)$

[a] The operation for the barotropic velocity in the cross-OB direction was described in the section 2.1, and the schemes for the baroclinic velocity in the cross- (U_b^{n+1}) and along-OB (V_b^{n+1}) directions, as well as active tracers (T_b^{n+1}) are presented in the table, respectively. The subscripts R and T stand for the subtidal and tidal velocity. l and g represent the local and global solution. n is the current time level, and b denotes the grid point at OB.

way, the parent domain provided the "*external data.*" We performed a harmonic analysis using the T-TIDE scheme in *Pawlowicz et al*. [2002] to obtain the *external* surface elevation and barotropic velocities at the OBs of the child domain from the solutions of the parent domain. We performed the decomposition of the tidal and subtidal currents off-line (Table 2). We stored the resultant harmonic constants, and we applied them to predict the tidal current $\left(\bar{U}_{Tlb}^{n+1}\right)$ and elevation (η_{Tlb}^{n+1}) in the TST-OBC. We obtained the subtidal external elevation (η_{Rlb}^{n+1}) and barotropic current $(\bar{U}_{Rlb})$ for their residual components. To further reduce the imposed distortion, we smoothed the external barotropic current by a 2 day low-pass filter.

Thus, the *tidal current*, $\bar{U}_{Tb}^{n+1}$, in the TST-OBC can be solved by the FLA-OBC,

$$\bar{U}_{Tb}^{n+1}=\bar{U}_{Tlb}^{n+1}\pm\sqrt{\frac{g}{H}}(\eta_b^{n+1}-\eta_{Tlb}^{n+1}-\eta_{Rlb}^{n+1}), \tag{4}$$

in which, the term $\pm\sqrt{\frac{g}{H}}(\eta_b^{n+1}-\eta_{Tlb}^{n+1}-\eta_{Rlb}^{n+1})$ denotes the barotropic tidal velocity $(\bar{U}_{Tb}^{n+1})$ contributed by propagating external gravity waves. The "+" and "−" signs denote the southern (western) and northern (eastern) OBs, respectively. The definitions for η_b^{n+1}, η_{Tlb}^{n+1}, and η_{Rlb}^{n+1} are the same as in equation (3). Based on the Arakawa-C grid utilized in ROMS, the TST scheme adapted a central average to compute η_b at the $\bar{U}_b$

Table 2. Flow Chart Shows the Procedure to Retrieve the Barotropic Forcing at the OB of the Child Domain From External Data of the Parent Solutions in the TST-OBC

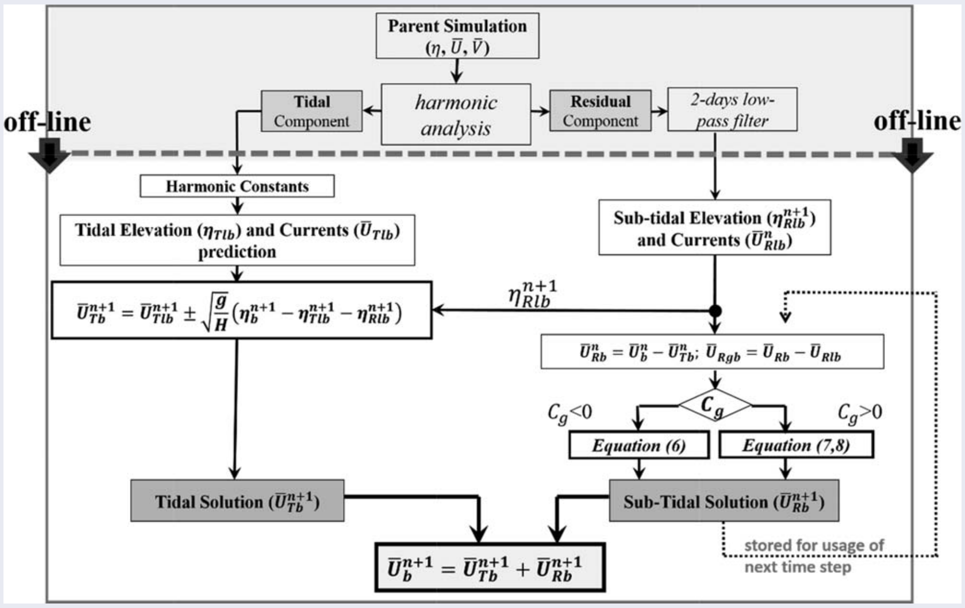

grid, which is sensible when radiation condition is applied to normal velocity instead of elevation [*Herzfeld*, 2009]. It was also favorable when η^{n+1}_{Tlb} and $\bar{U}^{n+1}_{Tlb}$ were well specified [*Carter and Merrifield*, 2007].

The *subtidal current* $\bar{U}^{n+1}_{Rb}$ is decomposed into local and global components (equation (2)). The local solution, $\bar{U}_{Rlb}$, represents the "*external data*." The global solution, $\bar{U}_{Rgb}$, represents the perturbation part of the subtidal velocity, $\bar{U}_{Rb}$, and it is computed from the Orlanski-type radiation condition that was implemented in ROMS [*Marchesiello et al*., 2001]. The phase speed (C_g) of a propagating disturbance is determined by:

$$C_g=\frac{\bar{U}^{n}_{Rg(b\pm1)}-\bar{U}^{n+1}_{Rg(b\pm1)}}{\bar{U}^{n+1}_{Rg(b\pm1)}-\bar{U}^{n+1}_{Rg(b\pm2)}}. \tag{5}$$

Thus, for the inflow condition ($C_g < 0$):

$$\bar{U}^{n+1}_{Rb}=\bar{U}^{n}_{Rb}-\frac{\Delta t}{\lambda}\left(\bar{U}^{n}_{Rb}-\bar{U}^{n}_{Rlb}\right), \tag{6}$$

and for the outflow condition ($C_g > 0$):

$$\bar{U}^{n+1}_{Rb}=\bar{U}^{n+1}_{Rlb}+\bar{U}^{n+1}_{Rgb}, \tag{7}$$

in which,

$$\bar{U}^{n+1}_{Rgb}=\frac{1}{1+C_g}\left(\bar{U}^{n}_{Rgb}+C_g\bar{U}^{n+1}_{Rg(b\pm1)}\right), \tag{8}$$

Δt is the time step of the external mode in ROMS. λ, which was 1.5 h in this study, acted as a relaxation time scale for the inflow condition.

We obtained the **total** barotropic, depth-averaged velocities perpendicular to the OB, by adding the tidal and subtidal velocities:

$$\bar{U}^{n+1}_{b}=\bar{U}^{n+1}_{Tb}+\bar{U}^{n+1}_{Rb} \tag{9}$$

We applied a no-gradient condition to the tangential velocity component ($\bar{V}^{n+1}_{b}$) and surface elevation (η_b) along the OB,

$$\bar{V}_b^{n+1}=\bar{V}_{b\pm1}^{n+1}. \tag{10}$$

$$\eta_b^{n+1}=\eta_{b\pm1}^{n+1}, \tag{11}$$

where the superscript, *n*, is the current time level, and *b* represents the boundary point. With the effectiveness of the TST-OBC, we found that the no-gradient condition performed reasonably better than a radiation condition or advective scheme for these variables in the applications discussed in the sections 4 and 5.

2.2. Baroclinic Currents and Active Tracers

We used equations similar to equations (4)–(9) to obtain the baroclinic normal velocity at the OBs. We obtained the local solution from the detided baroclinic velocities from the parent domains (also see Table 1). We deducted the tidal current ($\bar{U}_{TIb}$) to obtain the subtidal global solution, and then we added it back, after performing the above mentioned method (equations (5)–(8)) to obtain the total baroclinic normal velocity at the OBs. Thus, we applied the TST-OBCs to all the baroclinic variables to ensure consistency between the barotropic and baroclinic currents. This consistency is important for a model that applies the mode-splitting technique. We adopted a no-gradient OBC to solve for the baroclinic velocities in the along-OBs direction. We obtained the active tracers at the OBs from the algorithm similar to $\bar{U}_{Rb}^{n+1}$ (equations (5)–(8)), and the detided tracers field from the parent domain provided the local solution for active tracers in the child domain.

3. Ocean Model and Implementations

3.1. Numerical Implementation

We implemented the ROMS in the ECS, where the circulation is jointly driven by strong tidal and subtidal forces over complex topographies. We used a local closure scheme that was based on the level-2.5 turbulent kinetic energy equations [*Mellor and Yamada*, 1982], to parameterize the subgrid-scale vertical mixing processes in ROMS. A third-order, upwind-biased scheme solved the horizontal momentum advection. A multidimensional positive definite advection algorithm handled the advection of active tracers [*Smolarkiewicz*, 1984]. Horizontal diffusion for momentum and active tracers used a harmonic operator, and we set diffusivity and viscosity coefficients equal to 5 $m^2\ s^{-1}$.

The numerical model for the TST-OBC study included a small (child) domain embedded within a bigger (parent) domain. The TST-OBC connected the child domain with the parent domain. As a result, the solution in the child domain can be evaluated by comparing it with the baseline solution from the parent domain. To assess the performance of the TST-OBC, we conducted two groups of numerical experiments (Table 3) with identical child domains (CH-1 and CH-2), but different parent domains (PR-1 and PR-2) (Figure 1a).

The first group of experiments (group 1) contained simulations in the parent and child domains with identical horizontal resolution. The solutions from PR-1 were used as "*external data*" for the child experiments (CH-1). This set of experiments was designed to quantify the accuracy of the TST-OBC scheme in restoring the nature of the tidal and subtidal circulation in the child domain.

The second group (group 2) evaluated the adaptability of the TST-OBC in a downscaling application under variable forcing. In this group, we reduced the grid resolution extensively in the parent domain (PR-2), compared with PR-1, to fit the TST-OBC into a downscaling model. We conducted numerical experiments over the realistic ECS shelf topography, which is different from the previous OBC study that was based on the simplified shelf topography [*Chapman*, 1985; *Ma and Madsen*, 2011].

The horizontal grid and bathymetry in the computational domain are shown in Figure 1a, which displays the notable alongshore variations of the ECS bottom bathymetry and coastline. The parent domains (PR-1 and PR-2) extended alongshore ~1150 km from 25.8°N to 37.4°N, and offshore ~650 km from 119°E to 125.5°E. The eastward elongated coastline of the Shandong Peninsula formed a semiclosed northern boundary in the parent domain. A boundary fitted, orthogonal curvilinear grid with a (1241,448) dimensional array formed the horizontal mesh (x, y) of the parent domain (Table 3). We used variable horizontal grid spacing with a higher resolution ($\Delta x,\ \Delta y \approx 0.2 \sim 0.4$ km) from the coastal region to the 30 m isobath offshore in PR-1. It increased to ~1.5 km in the open ocean. We used a much lower (~4 times) horizontal resolution ($\Delta x,\ \Delta y \approx 0.8 \sim 6.0$ km) for PR-2 in the group 2 experiments (Table 3) to examine the effect of the

Table 3. Summary of the Numerical Experiments[a]

Experiment Group	Case ID	$(\Delta x, \Delta y)_{min}$ (km)	$(\Delta x, \Delta y)_{max}$ (km)	Source of Boundary Tidally Forced	Source of Boundary Subtidally Forced	OBC		
						Southern	*Northern*	*Eastern*
1	***PR-1***	(0.2, 0.4)	(1.6, 1.7)	OTIS	2D sub-model	***TST***	Closed	FLA
	CH-1	(0.2, 0.4)	(1.6, 1.7)	***PR-1***	***PR-1***	***TST***	***TST***	***TST***
	CH-1-FLA	(0.2, 0.4)	(1.6, 1.7)	***PR-1***	***PR-1***	FLA	FLA	FLA
	CH-1-CLP	(0.2, 0.4)	(1.6, 1.7)	***PR-1***	***PR-1***	CLP	CLP	CLP
2	***PR-2***	**(0.8, 1.7)**	(6.0, 6.5)	OTIS	2D submodel	***TST***	Closed	FLA
	CH-2	(0.2, 0.4)	(1.6, 1.7)	***PR-1***	***PR-2***	***TST***	***TST***	***TST***
	CH-2-FLA	(0.2, 0.4)	(1.6, 1.7)	***PR-1***	***PR-2***	FLA	FLA	FLA

[a] The abbreviations PR and CH stand for parent and child experiments, respectively. Spatial coverage and connection of the PR and CH domains were exhibited in Figure 1a. The bathymetry and domain of the two-dimensional submodel, which was used to derive local solutions for the parent domains, are illustrated in Figure 1b. The FLA and CLP schemes were denoted by the equations (3) and (12), respectively.

TST-OBC on downscaling modeling. We defined the grid in the child domains, CH-1 and CH-2 (119°E to 124.6°E and 27.5°N to 34.9°N), as a (774,388) dimensional array. The water column in the study area had 30 vertically discretized σ levels (Figure 1b) on the stretched terrain-following coordinates (*s*-coordinate) with higher resolution (less than 1 m) in the surface and bottom boundary layers.

3.2. Dynamics Configuration

It was advantageous to initialize the model with horizontally homogenous temperature and salinity that were measured in August 2009, in the field. August 2009 was a period of upwelling in the ECS [*Liu and Gan*, 2014]. The initial values of the barotropic $(\bar{u}, \bar{v})$, baroclinic velocities (u, v), and surface elevation (η) were zero.

The parent model experiments (PR-1 and PR-2) contained southern and eastern OBs (Figure 1a), while there were three OBs in the child domains (CH-1 and CH-2). Different from those summarized in the Table 2 for the child domain, the detided cross-OB velocities provided the local solution, $\bar{U}_{Rlb}$, at the southern OB of the PR-1 and PR-2 domains. We obtained these velocities from a simultaneous simulation that used local cross-shelf two-dimensional (x, σ, t) submodels (Figure 1b) as in *Gan and Allen* [2005], in which we applied a periodic OBC to the northern and southern OB. We applied the FLA-OBC for the barotropic velocity, and the radiation condition for the baroclinic velocity and active tracers [*Marchesiello et al*., 2001], at the eastern OB where the influence from coastal waves was minimal.

To identify clearly the nature of the oceanic circulation in response to forcing in the ECS, we forced the model with a spatially uniform southeasterly wind stress (~0.02 Pa) that had a meridional component equal to 0.018 Pa and a zonal component equal to -0.0125 Pa. This wind stress represented the climatological summer wind in the ECS [*Chu et al*., 2005], and it was the major driving force for the subtidal circulation over the shelf.

The M_2 tide dominates the tidal forcing in the ECS [*Wu et al*., 2011]. We derived the tidally induced elevation and depth-averaged velocities from the harmonic constants that were based on the Oregon State University Tidal Inversion Software (OTIS) data set [*Egbert and Erofeeva*, 2002]. This data set was assimilated from long-term remotely sensed TOPEX/Poseidon Sea Level Anomaly (SLA) data and was well-validated at most of the tide gauges in both the ECS and the South China Sea [*Zu et al*., 2008].

Driven concurrently by the tidal and subtidal forces, all numerical experiments were run for 50 M_2 tidal cycles (~25.8 days). We averaged all the results over the 10th–50th tidal cycles to extract the subtidal circulation.

4. Validation of the TST-OBC

We compared the results from CH-1 with the baseline results from PR-1 for the group 1 experiment (Table 3) to validate the performance of the TST-OBC scheme. We examined how the coastal circulation in CH-1 model responded to the tidal and subtidal forcing, separately. If the TST-OBC performed well, we expected the solutions from CH-1 to equal those from PR-1. We also compared the results using the TST-OBC with those using the FLA-OBC. We found that combining equation (3) for barotropic velocity and a passive

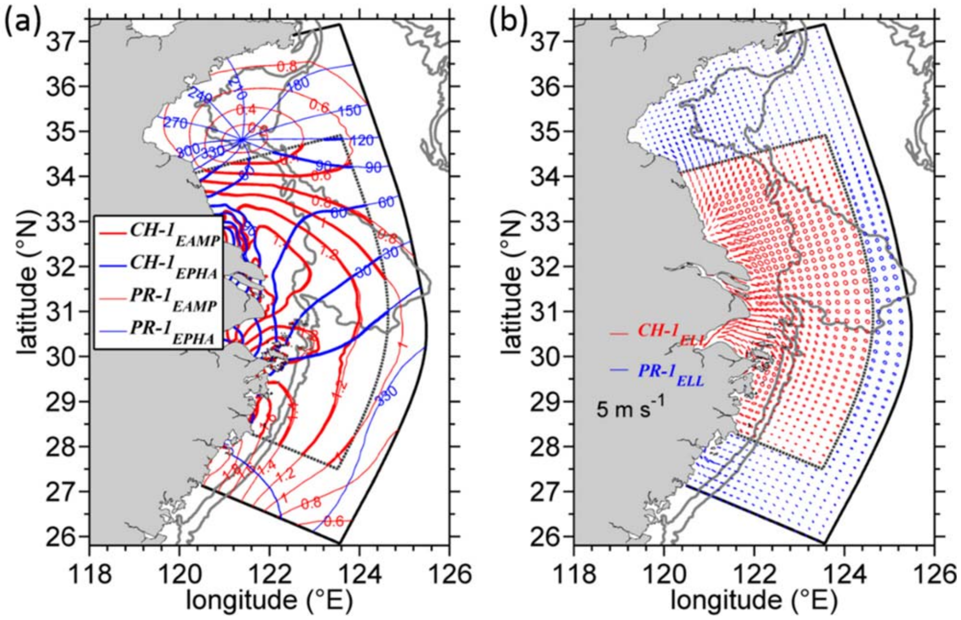

Figure 2. (a) Cotidal charts and (b) tidal current ellipses of the M_2 tide in the ECS. The thick/thin contours in Figure 2a represented solutions obtained from the child/parent domain experiments of CH-1/PR-1. The coamplitude (m) and cophase (°) lines were denoted by the blue and red contours, respectively. The red/blue ellipses in Figure 2b indicated the tidal ellipse from child/parent domain experiments of CH-1/PR-1, respectively. The 30 and 50m isobaths were shown by the grey bold lines.

radiation condition for the baroclinic velocity performed poorly compared to the results that we produced where we defined the FLA-OBC as follows: by using equation (3) for the barotropic velocity, and using the scheme proposed in section 2.2 for the baroclinic velocity.

4.1. Tidal Circulation

Horizontal maps of the cotidal chart and tidal current ellipses are shown in Figure 2. We computed the cotidal chart and ellipses using harmonic analysis [*Pawlowicz et al*., 2002] of the output of η and $(\bar{u},\bar{v})$ from PR-1 and CH-1. Referring to the PR-1 solution, accuracy of the TST-OBC scheme was quantified by measuring the domain-averaged relative errors in tidal amplitude, current magnitude, and phase and inclination angle of the ellipses between CH-1 and PR-1 (Table 4). To further estimate the effectiveness of the TST-OBC, we compared the solutions obtained from the TST-OBC with those obtained using the FLA-OBC and clamped (CLP-OBC) OBC in ROMS. This latter scheme fixed the boundary values to externally specified solution from PR-1 with:

$$\bar{U}_b^{n+1}=\bar{U}_{TIb}^{n}+\bar{U}_{RIb}^{n}. \tag{12}$$

The CH-1 solution generally agreed well with the PR-1 solution for all tidal variables (Figure 2). The solutions in both cases seamlessly linked with each other along their borders. Both of them had cyclonically traveling tidal waves (Figure 2a), which were also shown in *Lee et al*. [2002]. In addition, the solutions had shoreward elevated tidal amplitude. A distinct amphidromic point was located at a depth of ~30 m southwest of the Shandong coast. The tidal ellipses displayed a remarkable rotary current (Figure 2b) on the broad and shallow submarine delta east of the Jiangsu coast. The tidal current gradually transformed to a rectilinear flow west of the 30 m isobath, where the tidal energy increased considerably (Figure 2b).

The minimal relative errors (less than 1.8%, Table 4) in the tidal elevation and in the semimajor and semiminor axes of the ellipses demonstrate that the TST-OBC accommodated the tidal force along the OBs well. The tidal solution from the TST-OBC was very similar to that obtained with the FLA-OBC, and both solutions were much better than that from the CLP-OBC. There was also a negligible phase difference in the tidal current of ~4 min between CH-1 and PR-1, with high consistency in the inclination angle of tidal ellipses (Figure 2b).

Table 4. Summary of the Relative Errors in the Solutions Relative to the Baseline, PR-1, for the Tidal Elevation and Currents From CH-1, Using the TST-, FLA-, and CLP-OBCs, Respectively

Tidal Variables		TST-OBC	FLA-OBC	CLP-OBC
Elevation	*Amplitude*	1.59%	1.71%	1.81%
	Phase	0.02%	0.02%	0.04%
Current	*Semi-major axis*	1.46%	1.52%	1.58%
	Semi-minor axis	1.72%	1.55%	1.89%
	Phase	0.53%	0.55%	0.65%
	Inclination angle	0.11%	0.10%	0.21%

4.2. Subtidal Circulation

We present the horizontal distribution of the depth-averaged subtidal stream function (ψ) from experiments PR-1 in Figure 3a to illustrate the response of shelf current to the jointly imposed tidal and subtidal forces. Horizontal maps of depth-averaged subtidal kinetic energy (KE), velocity vectors, and relative vorticity (ξ) in the southwest region of the child domain are also displayed in Figure 3 to examine the TST-OBC's handling of the subtidal circulation at the OBs. Both the solutions from the parent domain outside the child domain and the solutions from the child domain itself are presented together to compare their consistencies.

In response to the summer monsoon in the ECS, a northward shelf current flows over the shelf between the 30 and 50 m isobath and crosses the southern OB of CH-1 (Figure 3a). This current weakens over the shelf at the northern OB of CH-1, where the waters are much shallower. There is no strong shelf current flowing across the eastern OB of CH-1. The child (CH-1 and CH-1-FLA, not shown) and parent (PR-1) solutions demonstrated a seamlessly connected ψ between them, indicating weak reflection by the TST-OBC and FLA-OBC. The northeastward subtidal circulation driven by the southeasterly monsoon and a southwestward counter-current near the 30 m isobath off the Zhejiang coast were consistently presented in all the solutions.

However, a detailed check of the velocity field, KE, and ξ in the southwest of the child domain, which was downstream of the alongshore propagating coastally trapped waves, suggests that the TST-OBC performed remarkably better than the more frequently used FLA-OBC. In CH-1, relatively strong KE (Figure 3b) occurred along the distinct upwelling jet (Figure 3c), where ξ (Figure 3d) was large. These variables translated smoothly from the PR-1 to the CH-1 domain across the southern OB of CH-1 when we used the TST-OBC. However, a remarkable accumulation of KE from reflective waves occurred at the southern boundary of the CH-1 domain when we used the FLA-OBC (Figure 3e). This portion of spurious KE increased the magnitude of the northeastward upwelling jet in the region around the 50 m isobath (Figure 3f), deflected the current mainstream eastward (Figure 3f), and created excessive disturbances (ξ, Figure 3g) in the interior solution. Obviously, the FLA-OBC was not handling the southward propagating coastally trapped waves very well as the waves crossed the southern OB of the CH-1 domain.

Figure 4 shows the cross-shore (x, z) sections of the alongshore velocity (v) and T along the northern OB, the central line, and the southern OB (Figure 3a) of the CH-1 domain using the TST-OBC. Both magnitude and structure of v and T in the upwelling circulation along these three transects, from CH-1 and PR-1, are highly consistent. CH-1 captured a strip of the northward alongshore upwelling jet well (Figure 4b) over the shelf, between the 30 and 50 m isobaths along the southern OB in PR-1 (Figure 4a). This region is where the deep waters are transported upslope and then outcrop in the surface layers over the inner shelf (Figure 4c).

The northeastward upwelling jet split into two strips in the central part of the ECS (Figures 4d and 4e) with an isolated deep cold water mass trapped in the central part of the ECS shelf (Figure 4f). This upwelling jet was suppressed considerably at the northern OB (Figures 4g and 4h), where strong tidal mixing suppressed an invasion of deep shelf waters (Figure 4i). Corresponding to the baroclinic density gradient from the upwelled shelf waters, a pronounced southward countercurrent formed beneath the mainstream of the upwelling jet. This countercurrent occurred between the 30 and 50 m isobaths from the northern to the southern OBs. All these features were qualitatively and quantitatively represented in both PR-1 and CH-1 solutions.

Figure 5 displays the time series of the domain-averaged subtidal KE, ξ, potential temperature change ($\Delta T = T(t) - T(t=0)$), and surface elevation (η_R) from the CH-1 and PR-1 solutions. A very small discrepancy in KE and ξ between two solutions, with their respective small relative error $e = 0.64\%$ and $e = 3\%$, suggests

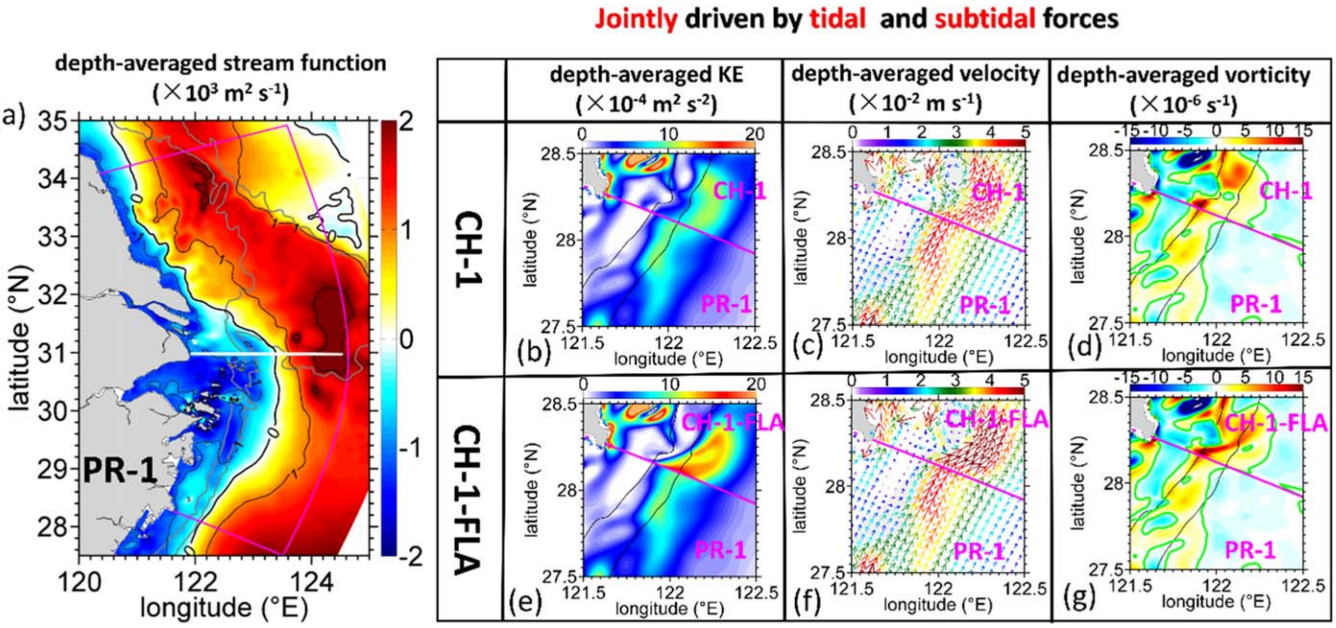

Figure 3. (a) Horizontal map of the depth-averaged subtidal stream function (ψ, $\times 10^3$ m^2 s^{-1}) from PR-1. (b) Depth-averaged, subtidal KE ($\times 10^{-4}$ m^2 s^{-2}), (c) velocity vectors ($\times 10^{-2}$ m s^{-1}), and (d) relative vorticity ($\times 10^{-6}$ s^{-1}) at the southwest region of the CH-1 domain. (e), (f), and (g) are the same as (b), (c), and (d), but for the solutions obtained from the CH-1-FLA experiment, respectively. Colorbars in Figures 3c and 3f exhibited the velocity magnitude. The model results were averaged during the 10th–50th tidal cycles, and the solutions from the parent domain outside the child domain were also included in all figures to show their consistency. The southern OB of the child domains was marked by the pink solid line. A zonal transect that crosses the waters off CJE (central part of the CH-1 domain) was indicated by the thick white line in Figure 3a.

that the TST-OBC in CH-1 linked the flow well through the OB between PR-1 and CH1, and that it efficiently accommodated the propagation of disturbances across the OBs. In addition, the time series of η_R (Figure 5d) and ΔT (Figure 5c) from CH-1 suggests that the baseline solution in the barotropic and baroclinic fields were restored.

To identify the response of each component in the TST-OBC to the flow across the OB, we compared the time series of the section-integrated subtidal transports (Tr_R) normal to the northern, southern, and eastern OBs of CH-1 with the corresponding transports of PR-1 (Figure 6). We considered the contributions from the local transport (Tr_{Rl}), global subtidal transport (Tr_{Rg}), and the global tidal transport (Tr_{Tg}) to the total solution (Tr_R) of CH-1. We computed the two global transports using the radiation scheme (section 2), under the outflow condition. The total solution, for the subtidal currents from the CH-1 experiment, is expressed as: $Tr_R = Tr_{Rl} + Tr_{Tg} + Tr_{Rg}$. Our discussion focuses on the model outputs after the ramping-up period (0–9th cycles) of the tidal forcing.

The total subtidal volume transport across the OBs (Tr_R) varied coherently with Tr_{Rl}, which ensured general agreement between the child and parent solutions as shown in Figure 6. Disturbances (Tr_{Tg}), due to the barotropic tidal waves propagating across the southern (0.01 Sv, Figure 6a) and eastern (-0.01 Sv, Figure 6c) OBs, were relatively small, but they accommodated smoothly the flow transition between CH-1 and PR-1. As compared with smaller Tr_{Rg} and Tr_{Tg} in the northern OB, larger values of these transports at the southern OB suggested that the majority of the disturbances that were generated in CH-1 traveled in the direction of Kelvin or coastally trapped waves, and propagated out of the computational domain through the southern OB. There were much larger Tr_{Tg} along the OBs when we used the FLA-OBC (not shown).

5. TST-OBC Application

We verified the feasibility of the TST-OBC to concurrently accommodate tidal and subtidal forces in section 4. In this section, we examine the OBC's performance in "off-line" downscaling applications (experiment group 2 in Table 3), which is crucial to multiscale oceanic modeling. We paid special attention to the subtidal circulation, for which unsatisfactory performance of OBCs has been frequently reported [*Ma and Madsen*, 2011].

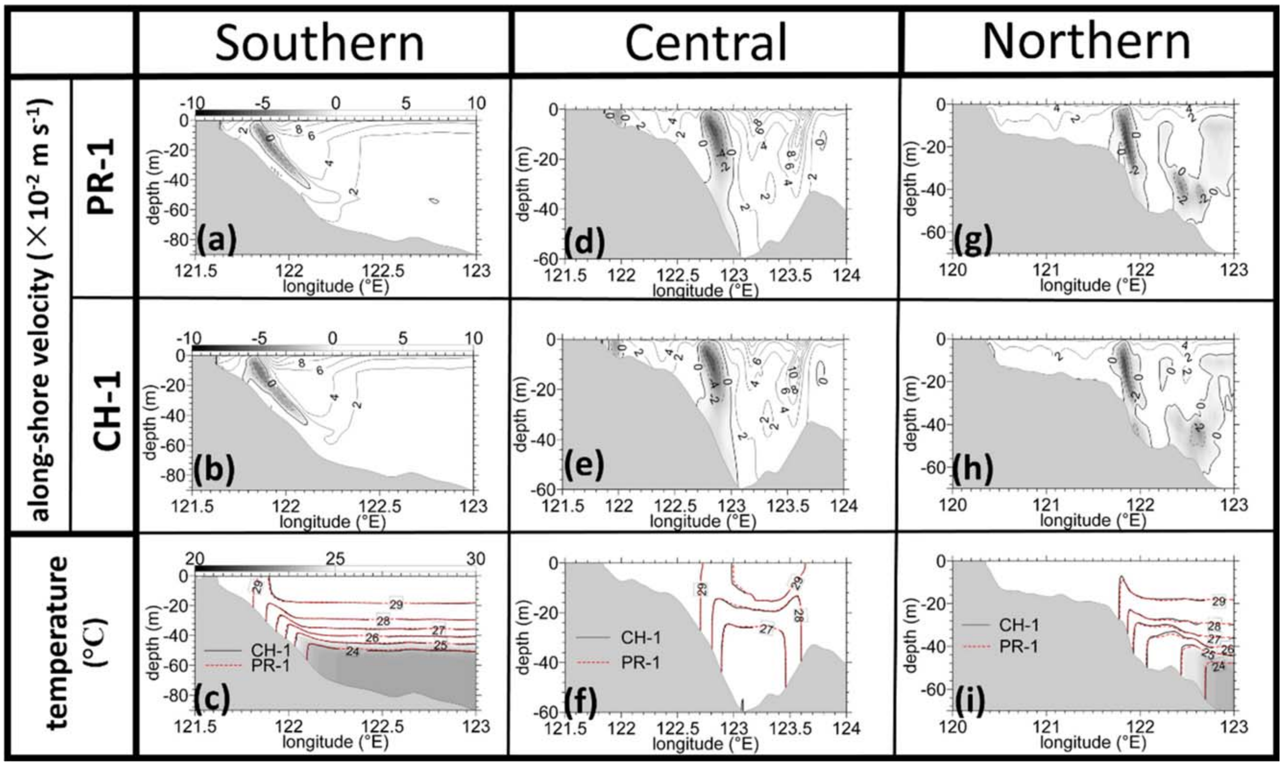

Figure 4. Across-shore sections of alongshore velocity v ($\times 10^{-2}$ m s^{-1}) from (a, d, g) PR-1 and (b, e, h) CH-1 solutions along the southern OB, the central line the northern OB of CH-1 domain, respectively. The across-shore sections of potential temperature (°C) obtained from the CH-1 (solid contours) and PR-1 (dashed contours) along the three-transects were illustrated in Figures 4c, 4f, and 4i, respectively. The model results were averaged during the 10–50th tidal cycles.

The solutions from the parent domain (PR-2 in Table 3) provided the "*external data*" in this study. These solutions had a horizontal resolution lower than PR-1. We used the stationary output presented by *Mason et al*. [2010] to derive high-frequency (2-hourly) prognostic variables from PR-2 along the OBs of CH-2. All approaches were similar to those applied in the group 1 experiment. We also evaluated the solutions of CH-2 that used FLA-OBC (CH-2-FLA, Table 3) for comparison.

We conducted three sets of experiments to evaluate the adaptability of the TST-OBC scheme to three dynamical circumstances where the parent and child models were (a) solely tidally driven, (b) solely subtidally driven, and (c) jointly driven by subtidal and tidal forces. The horizontal maps of the depth-averaged subtidal stream function (ψ) from PR-2, the depth-averaged subtidal KE, velocity vectors, and ξ distributions on the shelf near the southern OB of CH-2 are shown in Figures (7 and 8), and 9 for the three forcing cases, respectively. Figure 10 shows the time series of the domain-averaged subtidal KE in the entire child domain (left) and on the shelf (right) immediately bordering the OBs within 10 grid points. We displayed the cross-shelf sections of subtidal KE from the PR-1, CH-2, and CH-2-FLA experiments along the southern OB of the child domain in Figure 11 to examine the response of three-dimensional flow to the OBC schemes.

The high-resolution model is important in multiscale modeling over complicated bathymetry. The PR-1 solution was tentatively thought to be more "realistic" than the PR-2 solution with a lower spatial resolution. Using the PR-2 solution might affect the performance of the TST-OBC and the solution in CH-2. Therefore, the results shown in this section also demonstrate the capability of the OBCs in tolerating the "*external data*" at lower resolution, which has generally been encountered in multiscale ocean modeling.

5.1. Solely Driven by Tidal Forces

We started with the scenario of a tidally driven coastal current. Horizontal maps of ψ from PR-2 (Figure 7a) reveal the different responses of the coastal current in the southern and northern half of the computational domain. A southwestward flowing subtidal current occurred along the 30 m isobath toward the Zhejiang coast where a seaward gradient of ψ was negative. The subtidal current in the northern half of the computational domain

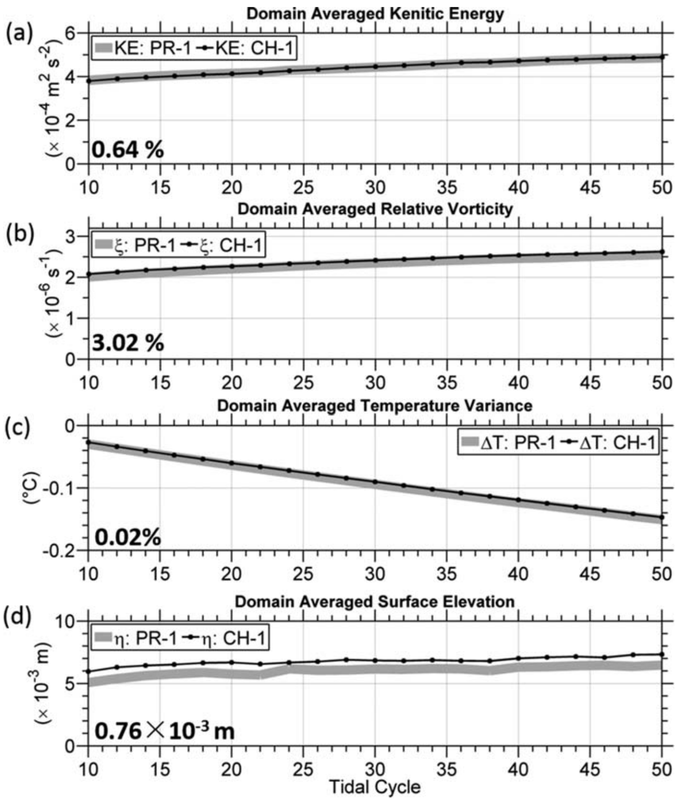

Figure 5. Time series of volume-averaged subtidal (a) KE, (b) relative vorticity (ξ), and (c) temperature change ($\Delta T = T(t) - T(t=0)$), (d) subtidal surface elevation from PR-1 (thick-gray lines) and CH-1 (thin-black lines), respectively. Solutions of PR-1 outside CH-1 domain were excluded. The numbers marked in Figures 5a, 5b, and 5c were the relative the errors between the solutions of CH-1 and those of the baseline (PR-1). The number in Figure 5d was the absolute error.

flowed northward on the shelf off the Jiangsu coast. Then the current circulated anticyclonically over the broad and shallow submarine delta northeast of the CJE. The circulation in CH-2, using the TST-OBC and CH-2-FLA (not shown), exhibited similar features to the circulation in PR-1. The similarity suggests that both OBCs performed reasonably well. These features were also exhibited in the domain-averaged KE in Figure 10a.

We examined the detailed response of the TST-OBC and the FLA-OBC. The TST-OBC scheme provided a smooth and continuous transition for the variables between the CH-2 and PR-2 solutions. The horizontal distributions of depth-averaged KE (Figure 7b), velocity vectors (Figure 7c), and ξ (Figure 7d) demonstrate this transition in the region near the southern OB. The converging KE toward the PR-1 solution within 10 grid points bordering the OBs also indicates a good performance of the TST-OBC (Figure 10b). This evidence indicates that the TST-OBC well links the signals between the low-resolution PR-2 and the CH-2, and it performs well in CH-2. In addition, the three-dimensional responses of the subtidal KE demonstrated that the TST-OBC performed better than the FLA-OBC (Figure 11b). Spurious disturbances along the southern OB were suppressed well in the TST-OBC results, and the CH-2 solution was restored towards the "*true*" solution in PR-1 (Figure 11a).

Although the FLA-OBC is "well-posed" at simulating the tidal current [*Carter and Merrifield*, 2007], it presented a problematic subtidal circulation in our downscaling application, even when the simulation was solely tidally forced. Despite the interior solution being restored toward the baseline solution (PR-1), the mainstream of the subtidal current in the southern half of the CH-2-FLA domain diverged offshore. This diverging current can be seen in the horizontal maps of depth-averaged subtidal KE (Figure 7e), velocity vectors (Figure 7f), and ξ (Figure 7g) on the shelf neighboring the southern OB. As a result, the southwestward coastal current off Zhejiang rebounded and moved offshore near the southern OB.

The time series of subtidal KE, averaged in the whole CH-2 domain and within 10 grid points bordering the OBs, demonstrated a similar discrepancy between the CH-2-FLA solution and the "*true*" solution in PR-1 (Figure 10). The discrepancy was due to the use of the FLA-OBC, and the unsatisfactory performance of the FLA-OBC also affected the spatial structure of flow field in the cross-shelf section of subtidal KE along the southern OB in Figure 11c. The KE of the subtidal baroclinic current from the case using FLA-OBC was much smaller than the expected KE in the PR-1 solution (Figure 11a). These findings indicated that, without fully considering the propagation of all disturbances, the subtidal KE obtained by the FLA-OBC notably drifted from the solution of PR-1 (Figure 11a).

5.2. Solely Driven by Subtidal Forces

In this section, we examine the performance of the TST-OBC scheme under subtidal southeasterly wind stress forcing. All the variables discussed in the previous section are illustrated in Figures 8, 10c, and 10d.

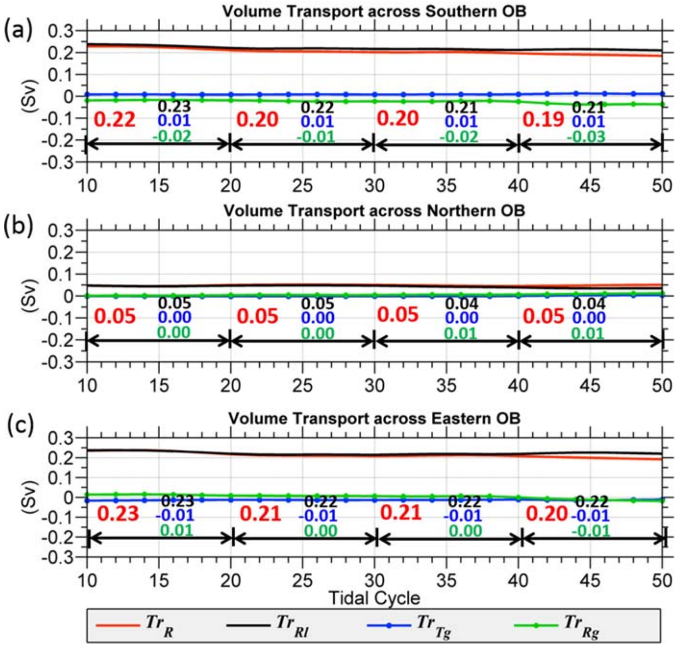

Figure 6. Time series of subtidal transport across the (a) southern, (b) northern, and (c) eastern OBs of the CH-1 domain. The total transports from CH-1 (Tr_R) and from PR-1(Tr_{RI}) were illustrated by the red and black lines, respectively. The transports across the OB associated with propagating tidal waves (Tr_{Tg}) and contributed by other disturbances (Tr_{Rg}) were shown by the blue and green lines, respectively. The values of transports at different time periods were marked in the respective figure.

Unlike the tidal forcing case, the circulation in PR-2 was qualitatively and quantitatively (Figures 10c and 10d), similar to that in PR-1, presumably because the subtidal current was less sensitive to the coarser topographic features resolved by PR-2. On the shelf, the upwelling-favorable wind stress established a strong northward coastal jet between the 30 and 50 m isobaths off the Zhejiang coast, and the coastal current in the submarine delta north of the ECS weakened (Figure 8a). The mainstream of the coastal jet deflected and rotated anticyclonically because of the squeezed vortex tube over the submarine delta [*Liu and Gan*, 2015].

The results of the TST-OBC scheme generally restored the CH-2 solution toward the solution of PR-1 in the flow field, depth-averaged KE (Figure 8b), velocity vectors (Figure 8c), and ξ (Figure 8d) on the neighboring shelf at the southern OB. It also reproduced the KE well in the entire computational domain (Figure 10c) and on the shelf that bordered the OBs (Figure 10d). The TST-OBC scheme proved to be capable of reconstructing the baroclinic flow by producing the consistent subtidal KE, with minimal discrepancy, along the southern OB between the PR-1 and CH-2 results (Figures 11d and 11e).

Generally, the FLA-OBC (CH-2-FLA) performed well, due to its *characteristic* property. However, it tended to produce KE noises near the southern OB (Figure 8e), and it imposed a stronger offshore displacement of the northeastward coastal current (Figures 8f and 8g). Although the domain-averaged barotropic KE was very similar between CH-2 and CH-2-FLA (Figure 10c), there was a larger deviation of the KE from PR-1 near the OBs in the case of CH-2-FLA. The reflected KE induced this deviation (Figure 10d). The cross-shelf section of the subtidal KE along the southern OB had even larger accumulative and reflective KE (Figure 11f). The solution obtained with the FLA-OBC illustrated a much stronger subtidal KE than the PR-1 solution (Figure 11d).

5.3. Jointly Driven by Tidal and Subtidal Forces

The responses and characteristics of the circulation jointly driven by tidal and subtidal forces are shown in Figures 9, 10e, and 10f. The horizontal distribution of ψ from PR-1 (Figure 3a) and PR-2 (Figure 9a) suggested general similarity between the two solutions, but PR-2 has a less energetic coastal current (Figure 10e), particularly at the central part of the eastern OB (Figured 9a, and 10f). Moreover, the monotonically eastward enlarging ψ on the shelf east of the Zhejiang coast in PR-2 (Figure 9a) indicated an absence of the notable southwestward counter-current (section 4 and Figure 3a) due to PR-2's lower horizontal resolution. The flow patterns were qualitatively consistent with the flow patterns of the previous cases that were solely driven by subtidal forces (Figure 8a), which reflected the dominant upwelling circulation in the study area.

The similarity between the PR-1 and CH-2 solutions for the averaged subtidal KE in the entire child domain (Figure 10e) and on the shelf bordering the OBs (Figure 10f) demonstrated good performance of the TST-OBC scheme. Consistent with the previous findings, the solutions of PR-2 and CH-2 agreed well at the southern OB (Figures 9b–9d) where most of the disturbances propagated through the OBs (Figure 6a) and there was not notable spurious reflection and accumulation of disturbances. Although the ψ field between CH-2

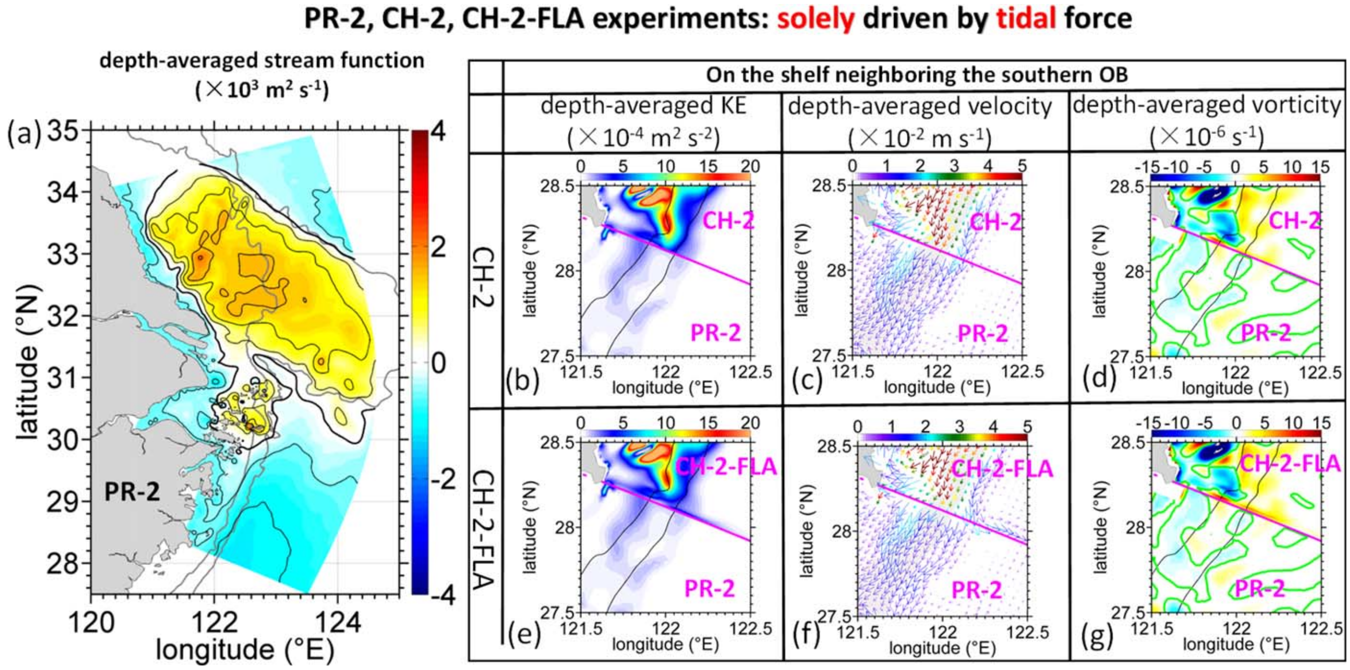

Figure 7. (a) Horizontal distributions of the depth-averaged subtidal stream function (ψ, $\times 10^3$ m^2 s^{-1}) from PR-2, and the depth-averaged, subtidal (b) KE ($\times 10^{-4}$ m^2 s^{-2}), (c) velocity vectors ($\times 10^{-2}$ m s^{-1}), and (d) relative vorticity ($\times 10^{-6}$ s^{-1}) at the southwest region of the CH-2 domain. Depth-averaged, subtidal KE ($\times 10^{-4}$ m^2 s^{-2}), velocity vectors ($\times 10^{-2}$ m s^{-1}), and relative vorticity ($\times 10^{-6}$ s^{-1}) from the CH-2-FLA experiment were presented in Figures 7e, 7f, and 7g, respectively. Colorbars in Figures 7c and 7f indicated the velocity magnitude ($\times 10^{-2}$ m s^{-1}). The model results were averaged during the 10–50th tidal cycles. The solutions from the parent domain outside the child domain were also included in Figures 7b–7g to show their consistency with those from CH-2. The OB of the child domain was marked by the pink solid lines in Figures 7b–7g, and the coastal current was solely driven by tidal force.

and CH-2-FLA looked similar, there were remarkable discrepancies between these two cases in the depth-averaged subtidal KE (Figure 9e), velocity vectors (Figure 9f), and ξ (Figure 9g) on the shelf neighboring the southern OB. The mainstream of the northeastward coastal current deflected eastward and considerable

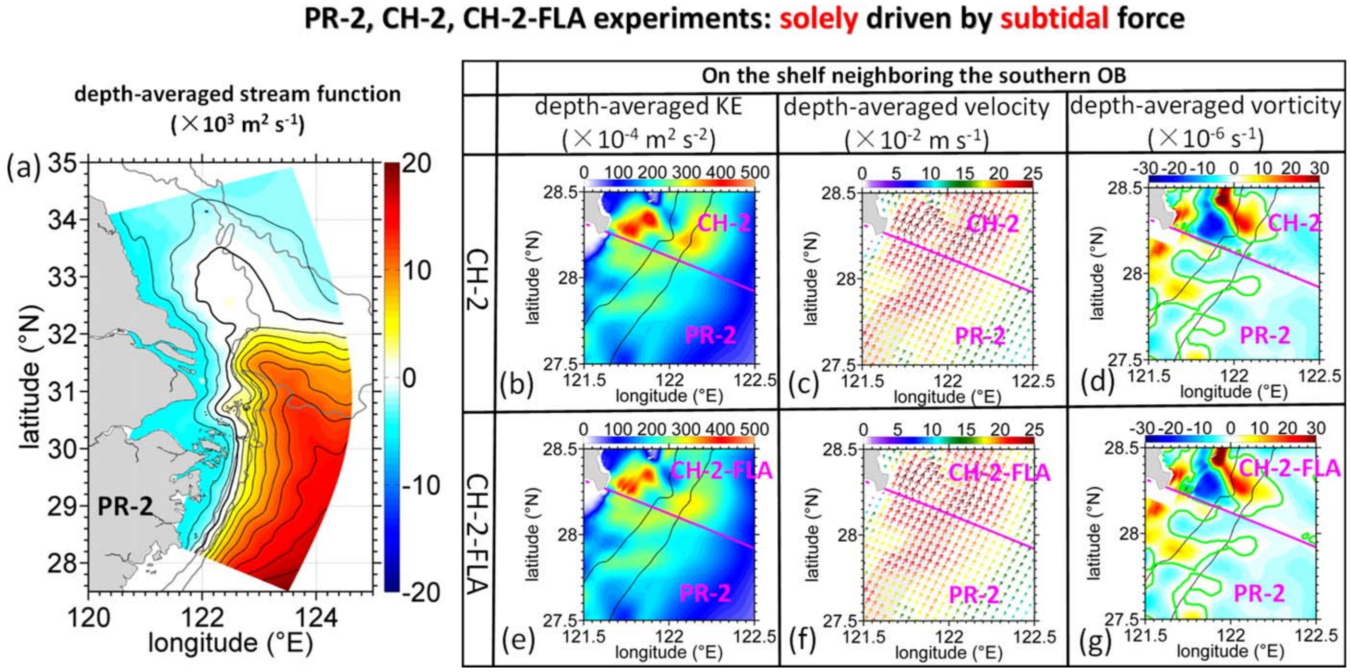

Figure 8. Same as Figure 7, but for the experiment solely driven by subtidal force.

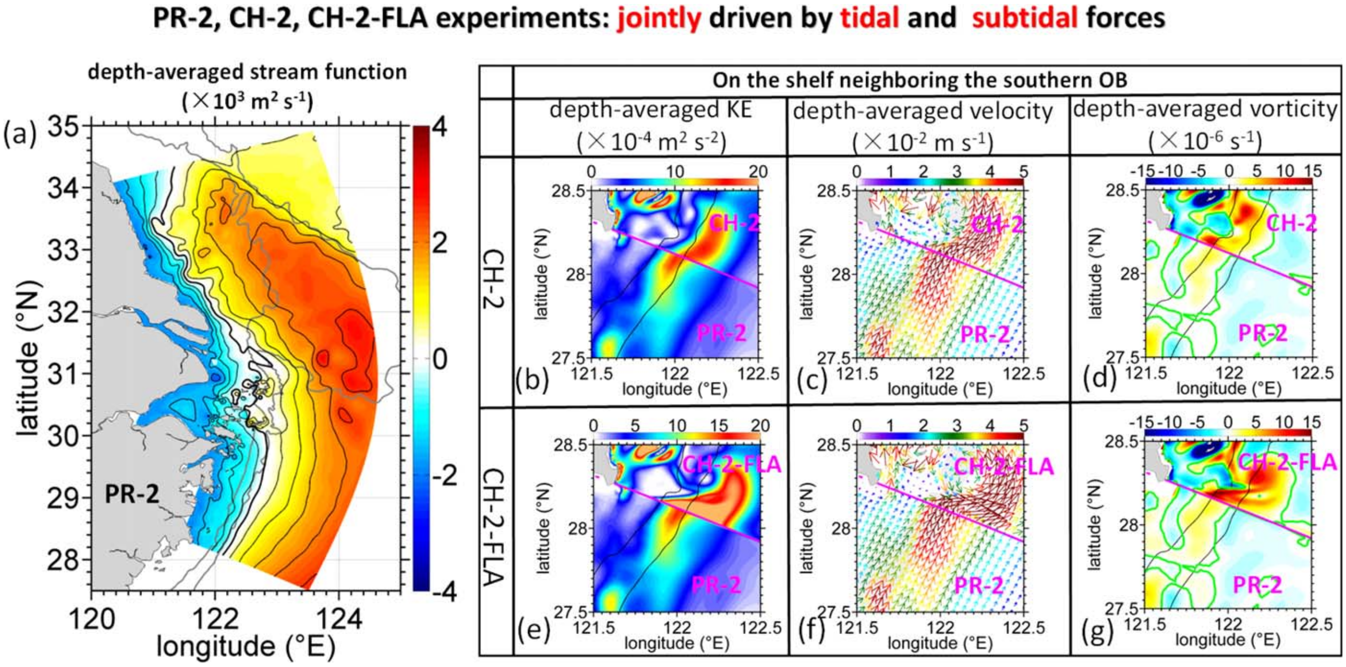

Figure 9. Same as Figure 7, but for the experiment jointly driven by tidal and subtidal forces.

spurious KE accumulated at the OB due to reflective disturbances. This spurious KE caused by the FLA-OBC was ~0.5 times stronger than the desired solution in PR-1 (Figure 10f).

We investigated the three-dimensional response of the flow field to the TST-OBC's tolerance to the "*external data*" at a lower resolution. The general consistency between the solutions by the TST-OBC (CH-2) and those from PR-1 was striking at first glance (Figure 11g and 11h). Over the southern OB, the northward alongshore current from CH-2 showed both quantitative and qualitative consistency with the solutions of PR-1, and we also observed similar faithful consistency along the eastern and northern OBs (not shown). However, the

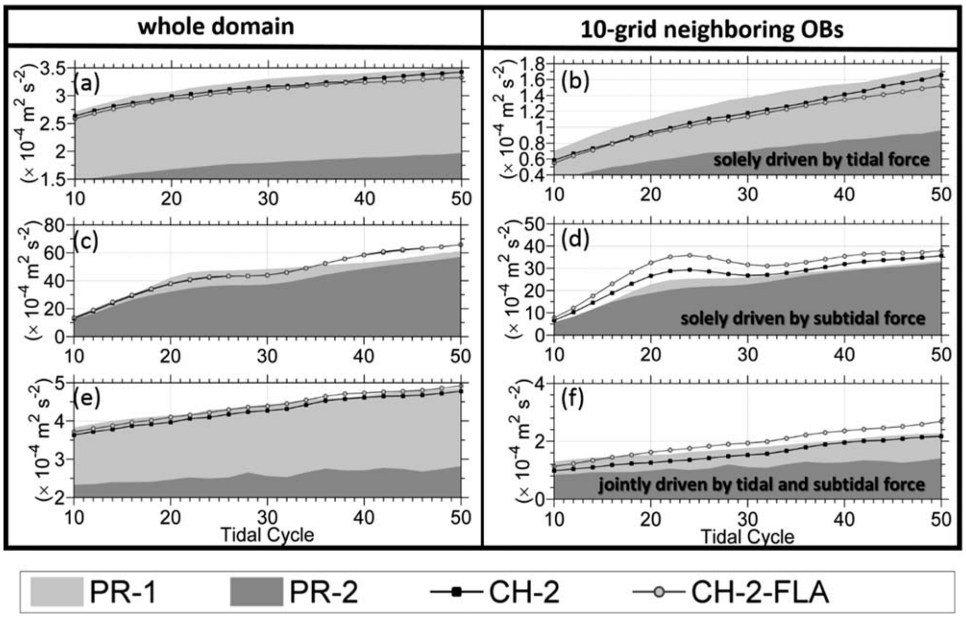

Figure 10. Time series of (left) domain-averaged subtidal KE from the experiments (a) solely driven by tidal force, (c) solely driven by subtidal force, and (e) jointly driven by tidal and subtidal forces. (right: b, d, f) The domain-averaged subtidal KE on the shelf within 10 grid neighboring all OBs of the CH-2 domain.

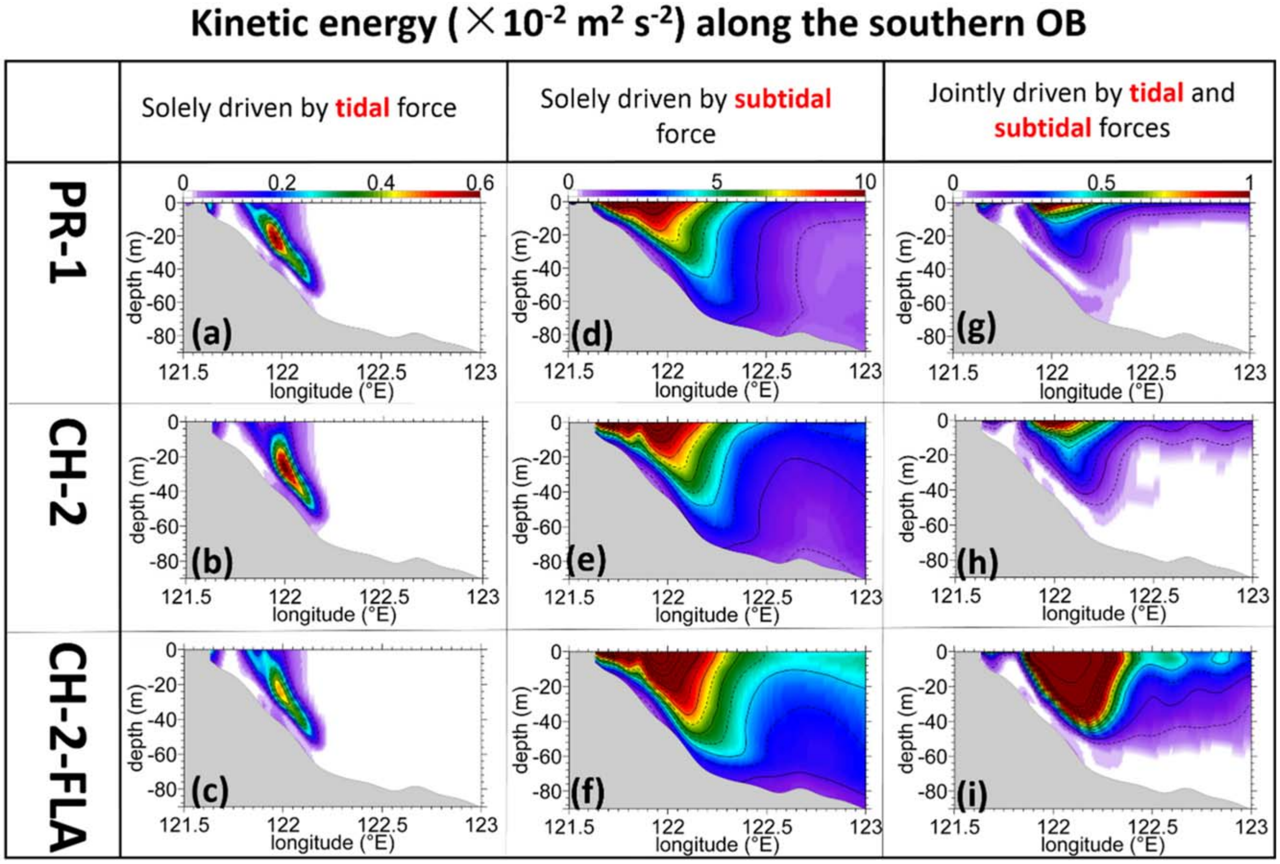

Figure 11. Cross-shore section of (left) kinetic energy ($\times 10^{-2}$ m^2 s^{-2}) along the southern OB of the child domain for the experiments (a, b, c) solely driven by tidal force, (d, e, f) solely driven by subtidal force, and (g, h, i) jointly driven by subtidal and tidal forces. The upper, mid, and lower plots showed the results from the PR-1, CH-2, and CH-2-FLAexperiments. The results were averaged during the 10–50th tidal cycles.

results from the FLA-OBC were unsatisfactory (Figure 11i). For the FLA-OBC, the subtidal KE over the southern OB had a great deal of spuriously reflected disturbances that deviated from the PR-1 solution (Figure 11g). The temporal evolution of depth-averaged subtidal KE on the shelf within 10 grid point bordering the OBs also showed that the FLA-OBC solution was not restored to the PR-1 solution (Figure 10f).

It is also worth noting that the solutions (not shown) obtained by the using radiation condition of *Mason et al.* [2010] showed notable improvement from the results by the FLA-OBC. However, they are still drifting from the expected PR-1 solution. This finding suggested a high-level dependency on the accuracy of "*external data*" in the OBC of *Mason et al.* [2010].

5.4. Response of the OBC to External Forcing

We have identified that the TST-OBC scheme performed well and that the FLA-OBC was potentially problematic under the dynamical condition of joint subtidal and tidal forcing. We further investigated the performance of these two schemes by analyzing the temporal evolution of the depth-averaged subtidal KE along the 50 m isobath. This selected isobath was perpendicular to the southern OB of CH-2 and extended northeastward to ~29°N, toward the Zhejiang coast (Figure 1a). In CH-2, the mainstream of the northward coastal current generally situates over this 50 m isobath (Figure 9b).

Figure 12 showed the KE of the depth-averaged velocity along the 50 m isobath from 28.1°N–29°N, north of the southern OB of CH-2. The result is based on snapshot outputs at 2 hourly intervals. We detided and low-pass filtered (2 day) the velocity to highlight the subtidal KE. We computed the power spectral density (PSD, right plot in Figure 12) with a Fast Fourier Transform (FFT) of the time series of depth-averaged subtidal KE along the 50 m isobath. Figure 13a shows the depth-averaged subtidal KE that was carried by the waves and disturbances with a period $>$ 2 days. The scattered dots in Figure 13b depict the time series of phase

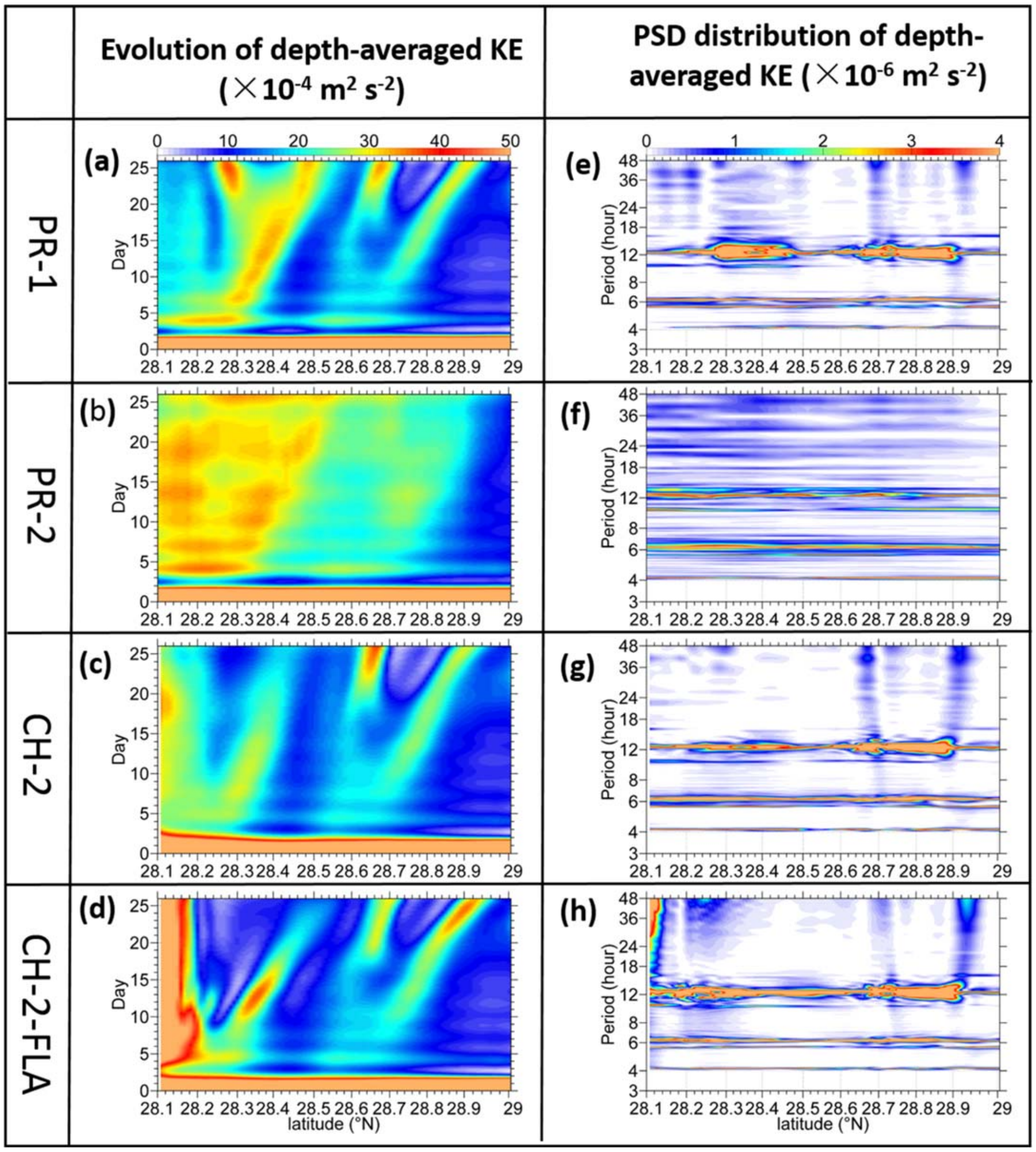

Figure 12. Temporal evolution of the depth-averaged, subtidal (left) KE ($\times 10^{-4}$ m^2 s^{-2}) along the 50 m isobath from 28.1–29°N north of the southern OB of CH-2. The results were from (a) PR-1, (b) PR-2, (c) CH-2, and (d) CH-2-FLA, respectively. The corresponding (right) PSD distribution over the 50 m isobath was illustrated in Figures 12e–12h coherently. The model was jointly driven by tidal and subtidal forces.

speed (C_g, equation (5)) solved by the TST-OBC along the 50 m isobath. We extracted C_g from the snapshot output of ROMS at 2 hourly intervals. The shaded curve in Figure 13b represents the low-pass (2-day) filtered phase speed at the southern OB of CH-2.

The external gravity waves associated with M_2, M_4, and M_6 tides excited the most energetic disturbances at the OB (right plot in Figure 12). There was a considerable difference in the KE evolution between the high (PR-1) and low-resolution (PR-2) experiments (Figures 12a, 12b, and 13a), and their associated PSD distributions are displayed in Figures 12e and 12f. Although the coastal current in the interior was much weaker in PR-2 (Figure 10e), its solution showed the presence of an intensified coastal current on the shelf near the southern OB (Figure 12b). We believe that a suppressed seaward baroclinic pressure gradient force (PGF) intensified the current due to reduced upslope transport of deep dense waters in PR-2. This then imposed the contaminated and strongly oscillating "*external data*" onto the intensified coastal current over the southern OB of the child experiments, CH-2 and CH-2-FLA (Figures 12f and 13).

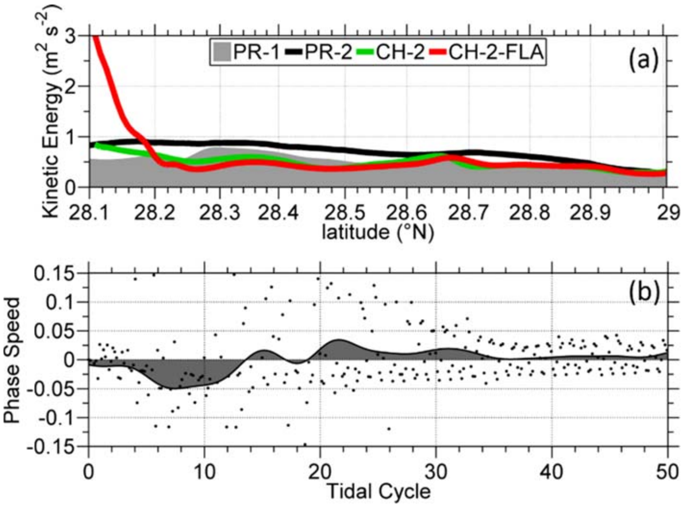

Figure 13. (a) Summation of the depth-averaged subtidal KE along the 50 m isobath for the disturbances varying in the period longer than 2 days, and (b) time series of the phase speed C_g (dots, equation (5)) from CH-2. In Figure 13b, the shaded curve exhibited the (2 day) low-pass filtered time series of C_g. The models were jointly driven by tidal and subtidal forces.

This contaminated "*external data*" was largely suppressed by using the physically sensible TST-OBC at the OB, as shown in Figure 11h. The subtidal KE along the 50 m isobath (Figures 12c and 12d) shows that the model responded differently to the inflow/outflow of this contaminated "*external data*" by the TST-OBC and FLA-OBC. For the FLA-OBC, there was considerable reflection and accumulation of the spurious KE on the shelf neighboring the southern OB (Figure 12d) because the outflow conflicted with the forcing of the OBC. This resultant inconsistency is also defined as an overspecification problem in *Marchesiello et al.* [2001]. As a result, waves and disturbances arriving at this OB were greatly amplified (Figure 13a), and they generated variations at a wide range of periods (Figure 12h). The interior solution, on the shelf off the Zhejiang coast, dramatically drifted away from the expected "*true*" solution of PR-1.

The TST-OBC performed much better than the FLA-OBC. The subtidal KE (Figure 12c) in CH-2, near the southern OB, was consistent with that in PR-2 (Figure 12b), which allowed the disturbances in both high (Figure 12g) and low-frequencies (Figure 13a) to propagate out of the domain without significant reflection. The interior solution in CH-2 (Figure 12c) was able to converge toward the PR-1 solution (Figure 12a) over a short distance (~20 km) away from the southern OB (Figure 13a). The TST-OBC was conceivably better adapted to the concurrent tidal and subtidal forcing at the OB than the FLA-OBC.

We further examined the performance of the TST-OBC by analyzing the temporal evolution of C_g where the 50 m isobath crosses the southern OB of CH-2 (Figure 13b). Alternating outward and inward propagating disturbances occurred at the OB. The highly variable C_g reflected the complex dynamic processes in the limited-area coastal ocean model. Dominant inward propagating disturbances from the CH-2 domain existed before the 14th tidal cycle (~7 days) when the inflow condition occurred (Figure 13b, also see equation (6)). Afterward, the outflow condition (equation (7)) activated when the disturbances (e.g., coastally trapped waves) that were generated inside the CH-2 domain propagated southward across the southern OB. The TST-OBC treated the relatively high magnitude C_g well during the 14th–34th tidal cycle without a notable "fake" reflection (Figures 12g and 13a). The TST-OBC's ability to resolve the highly variable C_g might be why it was better than the FLA-OBC at handling the flow across the OB in the limited-area coastal model.

6. Summary

The present study was motivated by commonly found inconsistencies existing in the OBCs of limited-area modeling when the model was concurrently driven by tidal and subtidal forces along the open boundary. The inconsistencies were partly caused by a priori-based selection of varied OBCs and by different combinations of schemes for barotropic and baroclinic velocities and active tracers. In this study, we proposed a novel formulation of the TST-OBC to mitigate the inconsistencies. We assessed the scheme based on the results obtained from the limited-area modeling over the ECS continental shelf where both tidal and subtidal forcings are important.

TST-OBC scheme involved the separation of fast-moving tidally and slowly moving subtidally forced disturbances as well as the separation of forced and unforced components in the subtidal flow. We treated the tidal current with the FLA-OBC. For subtidal components, we decomposed the concerned prognostic variables into local (forced) and global (unforced) components, and we treated the disturbances that traveled into (inflow) and out (outflow) of the computational domain, separately. The phase speed of inward/outward propagating disturbances (inflow/outflow) was determined by the global solution based on the unforced wave equation. For outflow across the OB, the solutions at OB were obtained by an Orlanski-type radiation OBC. For an inflow condition, we implemented a flow relaxation scheme to integrate external subtidal forcing with the interior solution. This TST-OBC scheme was applied to all variables along the open boundaries to ensure the dynamic consistencies.

We compared the computational results obtained with the TST-OBC from the parent domain with those from the child domain that was nested within the parent domain. We also compared the performance of the TST-OBC with that of the FLA-OBC. We conducted a comprehensive evaluation of the TST-OBC in the ECS with concurrent tidal and subtidal forcing and their respective forcing. We found that the solutions using the TST-OBC obtained from the limited-area child domain reproduced the "*true*" solutions that were obtained from the parent domain, and the child domain solutions realistically captured the observed features reported in the ECS.

Both the TST-OBC and the FLA-OBC reproduced the tidal circulation well when we concurrently used subtidal and tidal forcing. The relative errors in tidal elevation and semimajor axes and semiminor axes of the tidal ellipses that the TST-OBC generated were limited within 1.8%, and the phase error was negligible ($\sim$4 min). As for the subtidal current, the TST-OBC achieved a smooth transition between the parent domain and child domain of the variables along the OB. The smooth transition meant that disturbances with different frequencies crossed the artificial OB without significant reflection. However, subtidal solutions obtained from the case using the FLA-OBC tended to accumulate KE from reflective waves along the OB downstream of the coastally trapped waves.

We examined the performance of the TST-OBC in a downscaling application under a representative dynamic forcing in the shelf sea. The parent domain provided the local solution with ($\sim$4 times) coarser horizontal resolution. We conducted a set of experiments to represent the dynamical scenarios: (1) solely tidally driven, (2) solely subtidally driven, and (3) concurrently tidally and subtidally driven. These experiments showed that the TST-OBC linked the solutions between the child and parent domains well, without forming reflective and spurious signals along the OB. As a result, the interior solution of the nested model was very close to the "*true*" solution obtained by the higher-resolution parent model. We found that there was an obvious accumulation of spurious subtidal KE when we used the FLA-OBC. This spurious KE amplified when tidal and subtidal forces drove the coastal current concurrently. Our analyses showed that the TST-OBC is capable of resolving the highly variable phases for subtidal inflow/outflow of both barotropic and baroclinic signals across the OB. The absence of this capability in FLA-OBC may be problematic when both subtidal and tidal forcing exist at the OB.

The newly developed TST-OBC scheme uses a physically sensible global component in an (unforced) radiation boundary condition for propagating disturbances, and resolves the subtidal inflow/outflow and tidal flow across the OB simultaneously. It can effectively mitigate the inconsistent adaptation of OBCs and performs well in the simulation of ocean circulation with a limited-area domain that is driven concurrently by tidal and subtidal forcing, either in the shallow shelf water or in the deep open ocean [*Gan et al*., 2016].

Acknowledgments
This research was supported by the National Basic Research Program (973) of China, under project 2015CB954004, and by the Hong Kong Research Grant Council, under projects N_HKUST627/13 and 16202514. The authors are grateful for the thoughtful comments and suggestions from the anonymous reviewers. We also thank Linlin Liang for computer programming support. The programs, codes, and data for this study are available from the corresponding author at email address: magan@ust.hk.

References

Blayo, E., and L. Debreu (2005), Revisiting open boundary conditions from the point of view of characteristic variables, *Ocean Modell.*, *9*(3), 231–252.

Carter, G. S., and M. A. Merrifield (2007), Open boundary conditions for regional tidal simulations, *Ocean Modell.*, *18*(3–4), 194–209, doi:10.1016/j.ocemod.2007.04.003.

Chapman, D. C. (1985), Numerical treatment of cross-shelf open boundaries in a Barotropic coastal ocean model, *J. Phys. Oceanogr.*, *15*(8), 1060–1075, doi:10.1175/1520-0485(1985)015 <1060:NTOCSO>2.0.CO;2.

Chu, P., Y. C. Chen, and A. Kuninaka (2005), Seasonal variability of the Yellow Sea/East China Sea surface fluxes and thermohaline structure, *Adv. Atmos. Sci.*, *22*(1), 1–20, doi:10.1007/BF02930865.

Egbert, G. D., and S. Y. Erofeeva (2002), Efficient inverse modeling of barotropic ocean tides, *J. Atmos. Oceanic Technol.*, *19*(2), 183–204, doi:10.1175/1520-0426(2002)019 <0183:EIMOBO>2.0.CO;2.

Flather, R. A. (1976), A tidal model of the northwest European continental shelf, *Mem. Soc. R. Sci. Liege*, *10*(6), 141–164.

Gan, J. P., and J. S. Allen (2005), On open boundary conditions for a limited-area coastal model off Oregon. Part 1: Response to idealized wind forcing, *Ocean Modell.*, *8*(1–2), 115–133, doi:10.1016/j.ocemod.2003.12.006.

Gan, J. P., J. S. Allen, and R. M. Samelson (2005), On open boundary conditions for a limited-area coastal model off Oregon. Part 2: Response to wind forcing from a regional mesoscale atmospheric model, *Ocean Modell.*, *8*(1–2), 155–173, doi:10.1016/j.ocemod.2003.12.007.

Gan, J. P., A. Cheung, X. G. Guo, and L. Li (2009a), Intensified upwelling over a widened shelf in the northeastern South China Sea, *J. Geophys. Res.*, *114*, C09019, doi:10.1029/2007JC004660.

Gan, J. P., L. Li, D. X. Wang, and X. G. Guo (2009b), Interaction of a river plume with coastal upwelling in the northeastern South China Sea, *Cont. Shelf Res.*, *29*(4), 728–740, doi:10.1016/j.csr.2008.12.002.

Gan J., Z. Liu, and L. Liang (2016), Numerical modeling of intrinsically and extrinsically forced seasonal circulation in the China Seas: A kinematic study, *J. Geophys. Res. Oceans*, *121*, doi:10.1002/2016JC011800.

Herzfeld, M. (2009), The role of numerical implementation on open boundary behaviour in limited area ocean models, *Ocean Modell.*, *27*(1-2), 18–32, doi:10.1016/j.ocemod.2008.10.008.

Herzfeld, M., and P. A. Gillibrand (2015), Active open boundary forcing using dual relaxation time-scales in downscaled ocean models, *Ocean Modell.*, *89*, 71–83, doi:10.1016/j.ocemod.2015.02.004.

Lee, H. J., K. T. Jung, J. K. So, and J. Y. Chung (2002), A three-dimensional mixed finite-difference Galerkin function model for the oceanic circulation in the Yellow Sea and the East China Sea in the presence of M2 tide, *Cont. Shelf Res.*, *22*(1), 67–91.

Liu, Z., and J. Gan (2014), Modeling study of variable upwelling circulation in the East China Sea: Response to a coastal promontory, *J. Phys. Oceanogr.*, *44*, 1078–1094, doi:10.1175/JPO-D-13-0170.

Liu, Z., and J. Gan (2015), Upwelling induced by the frictional stress curl and vertical squeezing of the vortex tube over a submerged valley in the East China Sea, *J. Geophys. Res. Oceans*, *120*, 2571–2587, doi:10.1002/2015JC010715.

Ma, P. F., and O. S. Madsen (2011), An open boundary condition for numerical coastal circulation models, *J. Phys. Oceanogr.*, *41*(12), 2363–2380, doi:10.1175/2011JPO4574.1.

Marchesiello, P., J. C. McWilliams, and A. Shchepetkin (2001), Open boundary conditions for long-term integration of regional oceanic models, *Ocean Modell.*, *3*(1-2), 1–20, doi:10.1016/S1463-5003(00)00013-5.

Mason, E., J. Molemaker, A. F. Shchepetkin, F. Colas, J. C. McWilliams, and P. Sangra (2010), Procedures for offline grid nesting in regional ocean models, *Ocean Modell.*, *35*(1–2), 1–15, doi:10.1016/j.ocemod.2010.05.007.

Mellor, G. L., and T. Yamada (1982), Development of a turbulence closure-model for geophysical fluid problems, *Rev. Geophys.*, *20*(4), 851–875, doi:10.1029/RG020i004p00851.

Oddo, P., and N. Pinardi (2008), Lateral open boundary conditions for nested limited area models: A scale selective approach, *Ocean Modell.*, *20*(2), 134–156, doi:10.1016/j.ocemod.2007.08.001.

Oliger, J., and A. Sundstrom (1978), Theoretical and practical aspects of some initial boundary-value problems in fluid-dynamics, *SIAM J. Appl. Math.*, *35*(3), 419–446, doi:10.1137/0135035.

Orlanski, I. (1976), A simple boundary condition for unbounded hyperbolic flows, *J. Comput. Phys.*, *21*(3), 251–269.

Pawlowicz, R., B. Beardsley, and S. Lentz (2002), Classical tidal harmonic analysis including error estimates in MATLAB using T-TIDE, *Comput. Geosci.*, *28*(8), 929–937, doi:10.1016/S0098-3004(02)00013-4.

Perkins, A. L., L. F. Smedstad, D. W. Blake, G. W. Heburn, and A. J. Wallcraft (1997), A new nested boundary condition for a primitive equation ocean model, *J. Geophys. Res.*, *102*(C2), 3483–3500, doi:10.1029/96JC03246.

Pringle, J. M., and E. P. Dever (2009), Dynamics of wind-driven upwelling and relaxation between Monterey Bay and Point Arena: Local-, regional-, and gyre-scale controls, *J. Geophys. Res.*, *114*, C07003, doi:10.1029/2008JC005016.

Reid, R. O., and B. R. Bodine (1968), Numerical model for storm surges in Galveston Bay, *J. Waterw. Harbors Div.*, *94*(1), 33–58.

Roed, L. P., and O. M. Smedstad (1984), Open boundary-conditions for forced waves in a rotating fluid, *SIAM J. Sci. Stat. Comput.*, *5*(2), 414–426.

Shchepetkin, A. F., and J. C. McWilliams (2005), The regional oceanic modeling system (ROMS): A split-explicit, free-surface, topography-following-coordinate oceanic model, *Ocean Modell.*, *9*(4), 347–404, doi:10.1016/j.ocemod.2004.08.002.

Smolarkiewicz, P. K. (1984), A fully multidimensional positive definite advection transport algorithm with small implicit diffusion, *J. Comput. Phys.*, *54*(2), 325–362, doi:10.1016/0021-9991(84)90121-9.

Sommerfeld, A. (1949), Partial differential equation in physics, in *Lectures on Theoretical Physics-Pure and Applied Mathematics*, p. 1, Academic, N. Y.

Wu, H., J. R. Zhu, J. Shen, and H. Wang (2011), Tidal modulation on the Changjiang River plume in summer, *J. Geophys. Res.*, *116*, C08017, doi:10.1029/2011JC007209.

Zu, T., J. Gan, and S. Y. Erofeeva (2008), Numerical study of the tide and tidal dynamics in the South China Sea, *Deep Sea Res., Part I*, *55*(2), 137–154, doi:10.1016/j.dsr.2007.10.007.